

APPLICATION OF ADAPTIVE OPTICS TO FLUORESCENCE MICROSCOPY

by

BENJAMIN A THOMAS

(Under the Direction of Peter Kner)

ABSTRACT

When imaging deep into tissue samples in fluorescence microscopy, refractive index differences in the sample, and the refractive index differences between the sample, immersion medium, and cover glass cause distortion in the optical signal. These distortions result in a loss of resolution and a decrease of the signal to noise ratio of the imaging system. The addition of Adaptive Optics to a fluorescent microscope offers a possible method to correct these aberrations and obtain high resolution images in thick tissue. Adaptive Optics systems work by sensing the wavefront of the incoming light, and then correcting the distortions in the wavefront through the use of an adjustable optical element, usually a deformable mirror. In this paper we discuss the design and implementation of a Shack-Hartmann Wavefront Sensor for a wide-field fluorescence microscope for the measurement and correction of wavefront aberrations caused by *C. elegans*.

INDEX WORDS: Adaptive Optics, Fluorescence Microscopy, *C. elegans*

WAVEFRONT MEASUREMENT AND CORRECTION IN FLUORESCENCE
MICROSCOPY WITH ADAPTIVE OPTICS

by

BENJAMIN A THOMAS

BS, University of Georgia, 2008

A Thesis Submitted to the Graduate Faculty of The University of Georgia in Partial Fulfillment
of the Requirements for the Degree

MASTER OF SCIENCE

ATHENS, GEORGIA

2011

© 2011

Benjamin A Thomas

All Rights Reserved

WAVEFRONT MEASUREMENT AND CORRECTION IN FLUORESCENCE
MICROSCOPY WITH ADAPTIVE OPTICS

by

BENJAMIN A THOMAS

Major Professor:	Peter Kner
Committee:	Mark Haidekker
	Susanne Ullrich

Electronic Version Approved:

Maureen Grasso
Dean of the Graduate School
The University of Georgia
August 2011

TABLE OF CONTENTS

CHAPTER	Page
1 INTRODUCTION	1
Purpose of Study	1
Significance.....	3
Organization of Thesis	4
2 BACKGROUND	5
Fluorescence Microscopy	5
History of Adaptive Optics	6
Deformable Mirrors	7
Image System Quality.....	8
PSF and Zernike Polynomials.....	9
Sources of Aberration	11
Wavefront Measurement.....	12
Introduction to the Shack-Hartmann Sensor.....	13
Introduction to <i>C elegans</i>	15
3 LITERATURE REVIEW	17
Adaptive Optics and Two-Photon Microscopy.....	17
Adaptive Optics and Confocal Microscopy	18
Adaptive Optics and Wide-Field Fluorescence Microscopy	19
4 OBJECTIVES	22

5	SHACK-HARTMANN SENSOR	23
	Components and Optical Setup.....	23
	Sensor Signal	24
6	WAVEFRONT CALCULATION	26
	Gradient Calculation	26
	Sorting Algorithm	28
	Wavefront Reconstruction	30
	Programming Software	34
7	DEFORMABLE MIRROR.....	36
8	SHACK-HARTMANN SENSOR CALIBRATION	38
	Wavefront Reconstruction Algorithm Testing.....	38
	Optical Alignment Calibration.....	40
9	TESTING OF ADAPTIVE OPTICS SYSTEM	46
	Adaptive Optics System Description	46
	Wavefront Correction Goals	48
	Correction of Defocus Aberrations	49
	Correction of Depth Aberrations	52
	Correction of Induced Aberrations	53
10	MEASUREMENT AND CORRECTION OF ABERRATIONS IN <i>C. elegans</i>	57
	Preparation of <i>C. elegans</i> Samples	57
	Measurement and Correction using Microbeads as “Guide Stars”	57
	Wavefront Measurement using GFP.....	60
11	CONCLUSIONS.....	64

REFERENCES.....65

CHAPTER 1:

INTRODUCTION

Purpose of Study

The resolution of images deep in thick tissue using wide-field fluorescence microscopy is limited due to optical aberrations. With an increase in resolution, scientists will be better able to study important questions involving molecular and cellular structures within deep tissue and study important questions for medical research such as the interaction of drugs with cancer cells. When imaging biological samples, the light through the sample is distorted. This distortion is caused by the three dimensional structure of the sample refractive index as well as the varying indices of refraction of the sample, cover glass, and the medium in which the sample is contained. Aberrations must be corrected in order to obtain a high resolution, deep tissue image. The answer to correcting these aberrations lies in the implementation of an adaptive optics system.

Adaptive Optics systems have been used in astronomy for years to correct aberrations caused by the earth's atmosphere in astronomical images captured from ground-based telescopes. A typical setup for an Adaptive Optics system is shown in Figure 1.1. Adaptive optics systems work by sensing the wavefront of the incoming light, and then correcting the distortions through the use of an optical correction element. This is accomplished by using a reference point or "guide star," which is typically a nearby star or a laser beacon [1]. The light from the "guide star" propagates through the same aberrating medium as the scientific target and provides a means to measure the distortion of the wavefront. The wavefront is typically measured using a

Shack-Hartmann Wavefront Sensor (SHWFS). The wavefront is then corrected by using an optical correction element, typically a deformable mirror. A deformable mirror is a mirror that is mounted on a piston array and controlled by a computer.

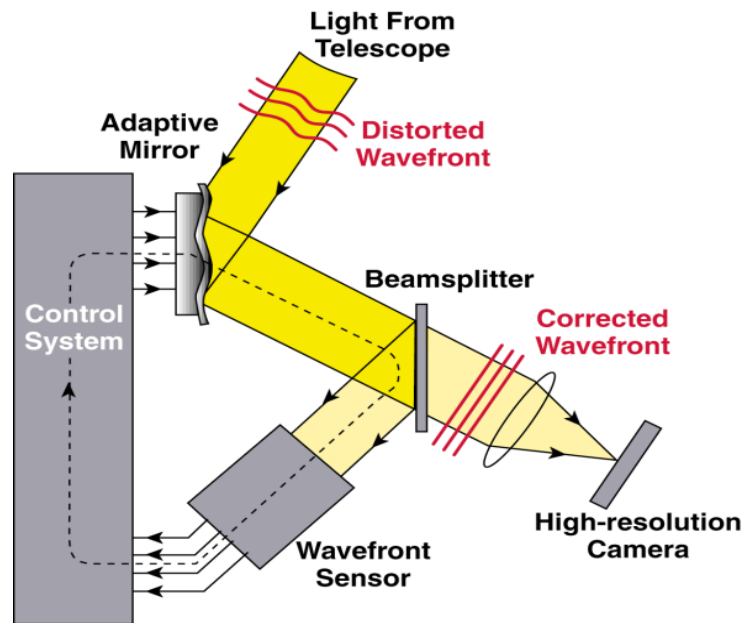


Figure 1.1: Diagram of a typical Adaptive Optics system [2].

The success of Adaptive Optics systems in astronomy has spurred research in its applications to microscopy. Over the past twelve years, Adaptive Optics systems have been successfully implemented in the fields of confocal [3, 29], multi-photon [4, 5, 19, 25, 26], and wide-field fluorescence microscopy [6, 7]. In systems developed for confocal and multi-photon microscopes, the wavefront sensor has been eliminated due to the lack of a suitable reference source or “guide star,” and indirect methods of aberration measurement are employed. Direct wavefront sensing has been accomplished in wide-field fluorescence microscopy using injected microbeads as the “guide star” for the sensor [7].

This study discusses the design and implementation of an Adaptive Optics system for use with a fluorescence microscope. The measurement and correction of aberrations caused by *C. elegans* will be investigated. We discuss the effectiveness of using microbeads as well as Green Fluorescent Proteins (GFP) as the "guide stars" for the Adaptive Optics system.

C. elegans (roundworms) are used to study a large variety of biological processes. These processes include cell signaling, gene regulation, metabolism, sex determination, disease related changes in the body, drug delivery and ageing [8, 9]. *C. elegans* is considered a model organism for humans due to the fact that the majority of human disease genes and pathways are present. They are a sophisticated multi-cellular animal that consists of various organs and tissues including muscle, skin, intestines, glands, reproductive systems, and a nervous system that are similar to organs and tissues in humans [8]. This easily cultured species is transparent, making it a suitable candidate for study using fluorescence microscopy.

Significance

The increase in resolution provided by implementing this Adaptive Optics system will allow biological studies on multi-cellular organisms to be performed in greater detail. This increase in resolution could benefit studies which involve measuring the shape and size of cells throughout an organism or studies investigating sub-cellular features. Successful measurement and correction of aberrations using GFP as the "guide star" of the system opens the door for obtaining corrected three dimensional models of the GFP expressing organisms.

This study also represents an important step towards obtaining corrected images of live, thick-tissue samples. Using various "guide stars" for wavefront measurement, we have demonstrated an improvement in image quality and simplified the wavefront measurement process in order to make this technology more accessible to Biologists.

Organization of Thesis

The thesis will begin with background information covering the history of Adaptive Optics, basic information on image system quality, the sources of aberration in microscopy, and background information on *C. elegans* (Chapter 2). Chapter 3 contains the Literature review and discusses previous applications of Adaptive Optics to various forms of microscopy. The objectives of this study are then presented in Chapter 4. Wavefront measurement is discussed in Chapters 5 and 6. Correction of the wavefront through the deformable mirror is discussed in Chapter 7. After reviewing the components of the Adaptive Optics system in Chapters 5-7, calibration of the wavefront sensor is discussed Chapter 8. Testing the Adaptive Optics system by correcting defocus and depth aberrations is presented in Chapter 9. Finally, the measurement of and correction of aberrations in *C. elegans* using microbeads as well as measurement of aberrations using GFP is discussed in Chapter 10.

CHAPTER 2

BACKGROUND

Fluorescence Microscopy

Fluorescence is the re-emission of light by a substance that has absorbed light at a shorter wavelength. Fluorophores (molecules which fluoresce) have been developed that are excited and emit light at specific wavelengths. These fluorophores can be attached to specific proteins. This is an important step in fluorescence microscopy, allowing specific proteins to be labeled. All proteins consist of the same 20 amino acids and are almost impossible to distinguish optically.

Fluorescence microscopes were first developed in the 1940s and work by exciting the fluorophores in the sample with the excitation light, then separating the fluorescent signal from the much stronger excitation light so that only light from the fluorophores is observed. Figure 2.1 displays a simplified fluorescence microscope setup. The excitation light and sample signal are separated by a dichroic mirror so that only the much weaker fluorescence signal will reach the CCD camera.

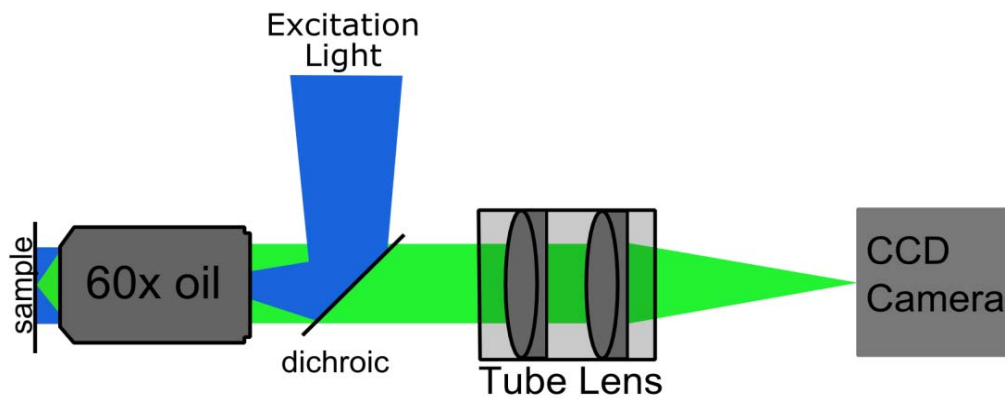
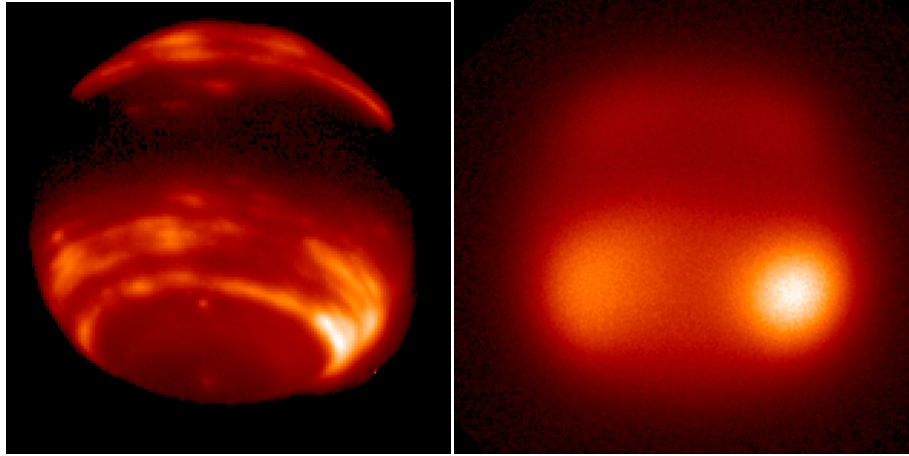


Figure 2.1: Fluorescence microscope basic setup

History of Adaptive Optics

The idea of Adaptive Optics was first developed for applications to astronomy. In 1953, Horace Babcock proposed using a deformable optical element along with a wavefront sensor to improve telescopic images. Babcock noted that without implementation of a system to correct for image aberrations caused by atmospheric turbulence, one was “fortunate to experience one hour out of 1000 of the finest seeing, even at the best locations” [10]. Adaptive Optics technology is based on the idea that the effects of an optical system can be altered by removing, adding, or altering the elements within the system [11]. Typically, a deformable mirror is used to as the correction element in Adaptive Optics systems. A deformable mirror consists of a reflected surface attached to an array of actuators that can modify the mirror shape.

Advancements in computer processing and micro-electro-mechanical systems have allowed the Babcock's idea to become a reality, and Adaptive Optics has since proven to be an effective method for optically correcting image aberrations. An example of the improvement in image quality from an Adaptive Optics system is displayed in Figure 2.2, which shows Neptune in infrared light with and without correction using Adaptive Optics [2].



a)

b)

Figure 2.2: Neptune in Infrared Light with (a) and without(b) adaptive optics [2]

Deformable Mirrors

A wide range of deformable mirrors have been developed for Adaptive Optics systems. Deformable mirrors have been manufactured to fit a wide variety of applications. The main types of these devices are segmented and continuous surface mirrors. Segmented deformable mirrors have rectangular or hexagonal reflective surfaces can be raised or lowered individually. They are capable of correcting for two-axis tilt by utilizing piezoelectric and hydraulic actuators. Continuous surface deformable mirrors consist of a flexible reflective surface that is attached to an actuator array. A comprehensive review of the basic technology and requirements of deformable mirror can be found in the paper by Freeman and Pearson [12].

Currently available Adaptive Optics elements have proven suitable for use in correction of microscopic images. The model presented by Kam et al. concluded that the spherical aberrations existing in these images can be corrected and that the correction involves only $2\mu\text{m}$ of correction for every $10\mu\text{m}$ of depth [13]. For a sample at a depth of $100\mu\text{m}$, the maximum movement of the actuators within the deformable mirror would need to be $20\mu\text{m}$. Current

manufactured deformable mirrors are capable of making this correction and can be purchased from companies such as Imagine Optic, Boston Micromachines, and OKO Technologies. The deformable mirrors available utilize micro-electromechanical, electrostatic, piezo, and magnetic actuators.

Image System Quality

When acquiring an optical image, it is desirable to obtain the best reproduction of the object possible. However, as light passes through an aperture, it bends. This is a phenomenon known as diffraction [14]. The diffraction limit is an inherent limit to optical resolution and is a result of the wave nature of light. Generally, if all of the elements of an optical system are perfect, then the resolution is said to be diffraction limited. The limitation of the resolution due to diffraction is inherent in Maxwell's equations for the propagation of light, and cannot be overcome. Therefore, the resolution potentially obtained in the optical system is limited [11].

The Point Spread Function (PSF) represents the image or intensity distribution of a point source of light. The Rayleigh criterion refers to the minimum resolvable detail. When the principle diffraction maximum of one Point-Spread-Function (PSF) coincides with the first minimum of the other, the two point sources are regarded as resolved. This is a measurement of resolution, which the Rayleigh criterion estimates based on the diameter of the aperture and wavelength of light. The diffraction limited resolution of a microscope can be calculated using Equation 2.1. The Numerical Aperture is a dimensionless quantity based on the maximum angle of light collection of the microscope objective (Equation 2.2); a higher numerical aperture corresponds to better resolution.

$$R = 0.61\lambda/NA \quad \text{Eq. (2.1)}$$

Where: R = Resolution, λ = wavelength, NA = numerical aperture

$$NA = n \sin(\theta) \quad \text{Eq. (2.2)}$$

Where: NA = numerical aperture, n = index of refraction of immersion medium of the object, θ = half angle of the maximum cone of light that can enter the lens

PSF and Zernike Polynomials

When evaluating the performance of an optical system, the size of the point spread function is the critical parameter [1]. The effect of wavefront aberrations on the PSF can be described using Fourier Optics. For a microscope objective, the plane one focal length in front of the lens is referred to as the focal plane while the plane one focal length behind the lens is referred to as the back pupil plane. Equation 2.3 relates the PSF and the back pupil plane [8]. $P(K_x, K_y)$ describes the aperture of the objective, where K_x and K_y are the x and y coordinates. $P(K_x, K_y)$ for a circular aperture is shown as Equation 2.4. When dealing with an imperfect system, the optical field is distorted and the equation for the PSF changes to Equation 2.5 [15].

$$PSF = \left| \int P(K_x, K_y) e^{iK_x x + iK_y y} dK_x dK_y \right|^2 \quad \text{Eq. (2.3)}$$

Where: $P(K_x, K_y)$ describes the aperture of the objective, K_x and K_y are spatial coordinates

$$P(K_x, K_y) = \begin{cases} 1 & \text{for } \sqrt{K_x^2 + K_y^2} \leq \frac{NA}{\lambda} \\ 0 & \text{for } \sqrt{K_x^2 + K_y^2} > \frac{NA}{\lambda} \end{cases} \quad \text{Eq. (2.4)}$$

Intensity distribution ($P(K_x, K_y)$) for a circular aperture. NA = numerical aperture, λ = wavelength, K_x and K_y are the x and y coordinates.

$$PSF = \left| \int P(K_x, K_y) e^{i\Phi(K_x, K_y)} e^{iK_x x + iK_y y} dK_x dK_y \right|^2 \quad \text{Eq. (2.5)}$$

Where $\Phi(K_x, K_y)$ describes the wavefront aberrations

Wavefront aberrations are described by $\Phi(K_x, K_y)$ in Equation 2.5. A common form of expressing aberrations in images is by expanding Φ in Zernike polynomials [16]. Zernike polynomials form a complete set on a unit circle, meaning that any aberration can be described as the sum of these polynomials [16]. The lowest orders of Zernike polynomials correspond to common optical aberrations such as: wavefront tilt, defocus, and astigmatism [1]. Zernike polynomials have been exceptionally useful in adaptive optics as a method of analytic evaluation of wavefront error [17].

Using the Zernike Polynomials corresponding to spherical aberrations (defocus) and astigmatism and Equation 2.3-2.5, the effect of these aberrations on the PSF was simulated. A horizontal profile showing the ideal PSF compared to the PSFs resulting from defocus and astigmatism with an amplitude of $\pi/2$ is shown in Figure 2.3. The ratio of the peak intensity measured in the presence of aberration divided by the intensity with no aberrations present is known as the Strehl ratio. In Figure 2.3 the Strehl ratio of the PSFs distorted by defocus and astigmatism are 0.41 and 0.62 respectively.

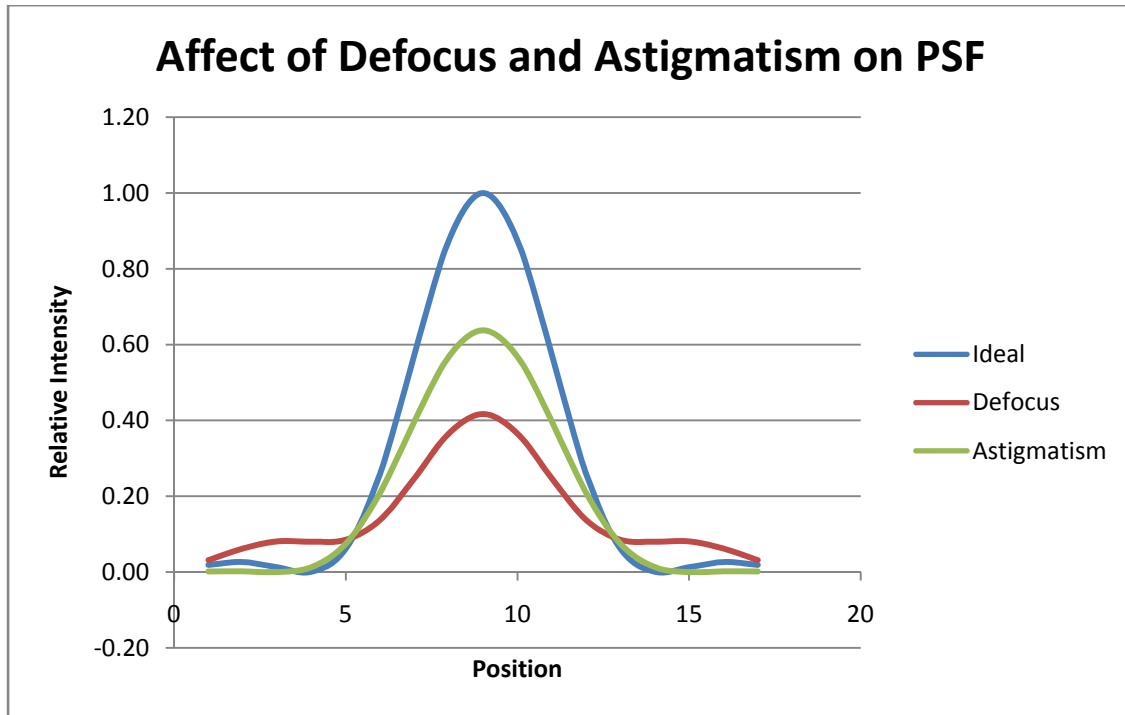


Figure 2.3: Ideal PSF compared to PSF distortions caused Defocus and Astigmatism aberrations at amplitude of $\pi/2$ radians

Sources of Aberration

Although the diffraction limit of an optical system cannot be breached, the images can be corrected for aberrations that prevent the imaging system from reaching its diffraction limit. Aberrations, in general, are distortions in image formation due to the optical system. In astronomy, aberration is experienced when light from a distant object becomes distorted by the varying refractive index of earth's atmosphere [1]. In microscopy, aberrations are caused by a number of factors. A major cause of aberration in microscopy is due to the varying refractive indices within specimens being studied [18]. The aberrations due to the shape of the specimen being studied tend to be dominated by low order Zernike modes, which are common optical distortions [18]. The low spatial frequency of these aberration modes means that they can be well corrected by deformable mirrors, which typically have more than 32 actuators.

When focusing into a sample, the maximum intensity of a point source decreases as depth increases, corresponding to a loss of resolution. This decrease in signal intensity is due to a mismatch in the refractive index of the sample and the immersion medium, these aberrations increase with depth according to Equation 2.6 [6, 19]. In live, complex, biological samples, which contain tissues and organs of varying refractive index, it is impossible to match the index of refraction of the immersion medium, resulting in spherical aberrations. Adaptive Optics techniques have been proven as a way to improve these PSF's and increase the resolution at depth [6, 8, 13].

$$\phi = 2\pi \frac{d}{\lambda} \left(n_2 \sqrt{1 - \left(\frac{(NA)\rho}{n_2} \right)^2} - n_1 \sqrt{1 - \left(\frac{(NA)\rho}{n_1} \right)^2} \right) \quad \text{Eq (2.6)}$$

Where: Φ = aberration, NA = Numerical aperture of optical system,
 n_1 = refractive index of sample, n_2 = refractive index of immersion medium, d = depth,
and ρ = normalized radial coordinate

Wavefront Measurement

Various techniques for measuring the wavefront of an optical system exist today such as the Foucault Knife Edge Test, Shearing Interferometer, Wavefront Curvature Sensor, and Shack-Hartmann Wavefront Sensor (SHWFS) [20, 21]. A SHWFS is easy to implement, compact, relatively insensitive to vibration, and provides accurate wavefront measurements. Wavefront sensors in adaptive optics systems have requirements that differ from optical interferometers used in laboratory testing [1]. For example, in laboratory interferometers, photon flux is abundant while measurement times are relaxed. However, in adaptive optics, sensors must operate with very low intensity signals at high speed in order to allow real-time correction [11].

Techniques for measuring the wavefront of a signal are often broken up into two categories: Zonal and Modal [1]. Zonal sensors directly measure the wavefront. To accomplish

the task of measuring a complex wavefront, the pupil is separated into an array of contiguous zones, or sub-apertures. In each zone, an independent measurement of the gradient, or slope, of the wavefront can be calculated and used to reconstruct the wavefront. Modal wavefront sensors operate by deducing the errors within the wavefront by their effect on a parameter, typically intensity, at the image plane. This type of sensing has shown success in confocal [3] and multiphoton microscopes [3, 4, 5, 22] and is frequently implemented due to the lack of reference sources or “guide stars” in the sample. These studies will be reviewed in greater detail in Chapter 3. Modal calculation of the wavefront requires the acquisition of several images, which can cause degradation of the final image due to photo-bleaching of the fluorescent label.

Introduction to the Shack-Hartmann sensor

The most commonly used sensor in astronomical adaptive optics has been the Shack-Hartmann Wavefront Sensor (SHWFS). In a SHWFS, an array of small lenses is used to create an array of images. The local gradient of the wavefront at each lens (lenslet) causes a lateral shift of the image (Figure 2.4). Typically a point source is imaged with a SHWFS, so the array of images created by the lenslets is an array of spots. The resulting position of each spot gives a direct indication of the local wavefront gradient at that sub-aperture [23]. An example of a Shack-Hartmann image is shown in Figure 2.5. The resulting measurements of the shift in spot position from the Shack-Hartmann image must be processed by a reconstructor to determine the wavefront.

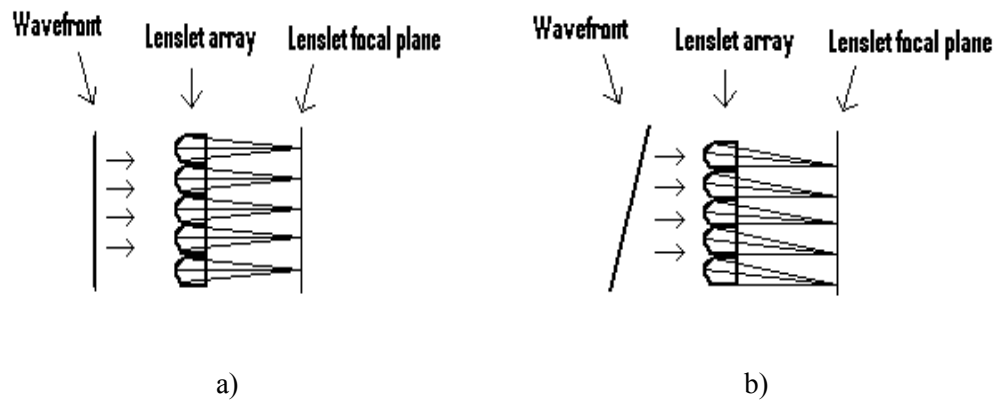


Figure 2.4: a) Flat wavefront shows no shifting of focal spots on lenslet focal plane, b) Shifted focal spots due to tilted wavefront.

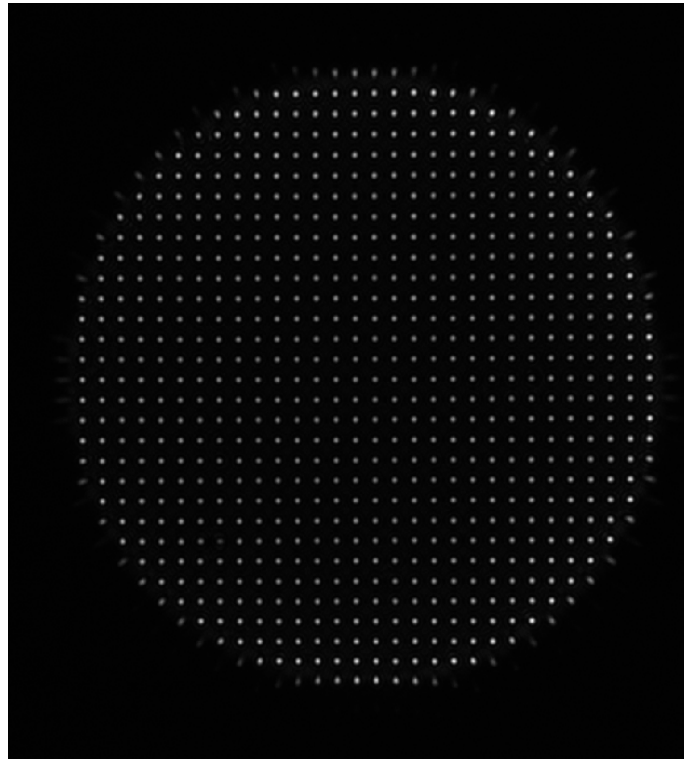


Figure 2.5: Shack-Hartmann Image

Introduction to *C. elegans*

Caenorhabditis elegans is a nematode commonly used for biological studies. Many biological processes can be studied in *C. elegans* including apoptosis, cell signaling, cell cycles, cell polarity, gene regulation, metabolism, ageing and sex determination [8]. It can be considered a model organism in that it can be used to study biological phenomena and lead to discoveries that could be applicable to other organisms. Previous studies have fully sequenced its genome and fully monitored all cellular divisions [24]. *C. elegans* is a sophisticated animal even though adult hermaphrodites only contain 959 somatic cells which form many different tissues and organs including muscle, skin, intestines, reproductive system, glands, and a nervous system. Not only do they share many similar tissue and organ types with humans, the majority of human disease genes and pathways are present in *C. elegans* [8].

C. elegans are transparent, easy to culture, and many strains already used in research express GFP. The adult *C. elegans* grows to a length of around 1mm and diameter of 60 microns, which is large enough to induce significant aberrations. These characteristics, as well as the numerous applications of *C. elegans* for biological study, make this nematode ideal as a test organism for the Adaptive Optics system. An example image of *C. elegans* in which the nerve system is labeled with Green Fluorescent Protein (GFP) is shown in Figure 2.6.

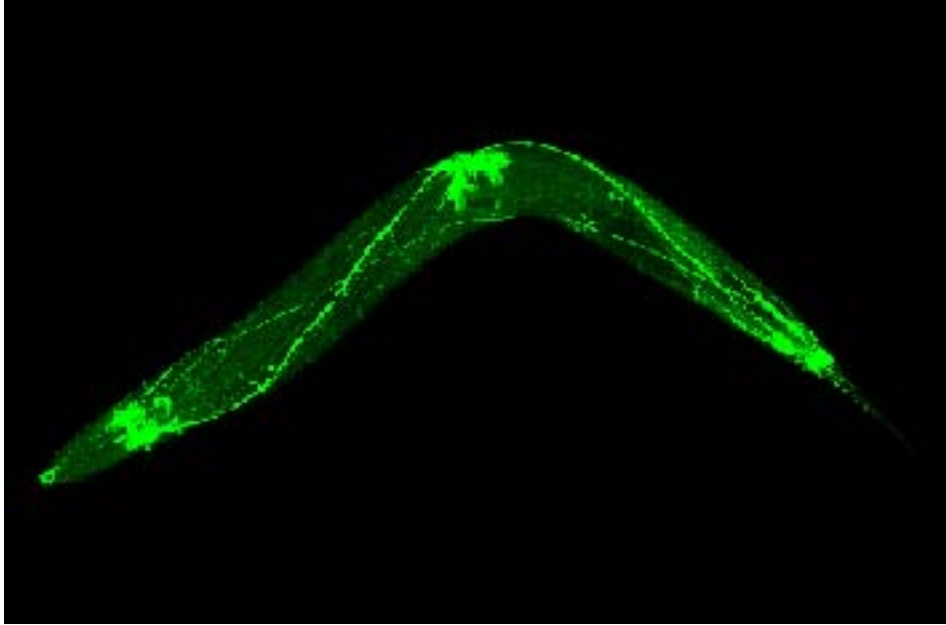


Figure 2.6: Fluorescently labeled nerve system in *C. elegans* [25]

CHAPTER 3

LITERATURE REVIEW

The effectiveness of adaptive optics technology applied to astronomy has been well documented [1]. It has also been applied to multi-photon [4, 5, 19, 26, 27], confocal [3, 30], and wide-field [6,7,13] fluorescence microscopy.

Adaptive Optics and Two-Photon Microscopy

The successful implementation of an Adaptive Optics system in two-photon microscopy was first accomplished by Albert et al. in 2000 [26]. Two-photon microscopy was developed in 1990 [28] and is based on the idea that two photons of low energy can excite a fluorophore by being simultaneously absorbed [29]. The probability of two photons being absorbed at the same time is extremely low, so a high concentration of excitation photons is necessary. A high temporal concentration of photons is achieved with a femto-second pulsed laser. Because two-photon excitation has a much higher probability of occurring within the tightly focused laser spot, out-of-focus fluorescence is not excited and does not need to be rejected with a pinhole as in single photon confocal microscopy. The fluorescence from the focal point is collected and the focal plane is scanned throughout the sample to form a complete image.

Neil et al. demonstrated that specimen induced aberrations could be corrected in two photon microscopy using adaptive optics [5] with a ferro-electric liquid crystal spatial light modulator (FLCSLM) to measure and correct wavefront aberrations. Aberrations were measured by a modal wavefront sensing technique, which measures and corrects individual Zernike aberration modes sequentially [22].

Rueckel et. al. demonstrated a focus near the diffraction limit using a coherence-gated wavefront sensor (CGWS) and deformable mirror to correct aberration in a two-photon fluorescence microscope. The CGWS uses back-scattered light to determine the wavefront, which allows low levels of excitation power to be used in the wavefront calculation [27].

In another two-photon system, Marsh et al. demonstrated the correction of specimen induced aberrations using a 15mm diameter Deformable Mirror. Optimization of the deformable mirror was based on the magnitude of the two-photon induced fluorescence signal, which required several scans of the sample. Using 105nm fluorescent microbeads, the attainable imaging depth was extended from 3.4 to 46.2 μm at a set resolution of a Full-Width-Half-Maximum (FWHM) of 1.25 μm . This study also demonstrated a 40 % increase in maximum signal as compared to an uncorrected image of smooth muscle from a guinea pig bladder [19]. A similar system developed by Sherman et al. [4] showed correction of depth induced aberrations by optimizing the shape of a deformable mirror using the feedback fluorescence and a genetic learning algorithm.

Adaptive Optics and Confocal Microscopy

An Adaptive Optics system has also been successfully implemented with a confocal microscope [3, 30]. Confocal microscopes utilize point illumination to increase optical resolution and contrast. This is accomplished through the use of a spatial pinhole which only allows light produced near the focal plane to be detected. The ability to optically section samples results in increased contrast, but limits the number of photons reaching the detector, which increases noise. Since only one point of the sample is imaged at a time, it necessary to scan the sample in order to produce a full 2D or 3D image.

The adaptive confocal microscope demonstrated by Booth et al. also employs a modal sensor which consists of the existing pinhole detector of the confocal microscope and a deformable mirror. The deformable mirror served as the correction element as well as the sensor biasing device. Wavefront aberrations were measured by applying Zernike aberration modes to the deformable mirror and using the effect of each mode on the wavefront to determine the overall aberration. Improved contrast and resolution were demonstrated in the X-Y and X-Z scans of fluorescently labeled mouse intestines [3].

A recent confocal system developed by Tao et al. demonstrated the high speed correction of aberrations by direct measurement of the wavefront with a Shack-Hartmann Wavefront Sensor and correction with a deformable mirror containing 140 actuators [30]. Fluorescent microbeads were fixed to the coverslip and slide to be used as the “guide star” for the Adaptive Optic system. A 240% increase in the signal intensity was observed while imaging mouse brain tissues at depths up to 100 μ m [30]. This system demonstrated that microbeads fixed beneath a sample could be used to measure wavefront aberrations in a confocal microscope.

The drawback of the two-photon systems and confocal system by Booth et al. is that wavefront aberrations are measured indirectly. Individually measuring the Zernike mode aberrations or optimizing the shape of the deformable mirror based on an image parameter requires the acquisition of several images. The lack of a means to directly measure the wavefront results in a system which operates slowly and is susceptible to photobleaching.

Adaptive Optics and wide-field fluorescence microscopy

Adaptive Optics has been successfully implemented in wide-field fluorescence microscopy [6,7,13]. A two-fold increase in signal intensity has been achieved using a deformable mirror as the optical correction element [13]. In this system, correction of depth

aberrations was performed by calculating the phase correction based on the mathematical equations for the path length differences, resulting in improvement of the point-spread function (Figure 3.1).

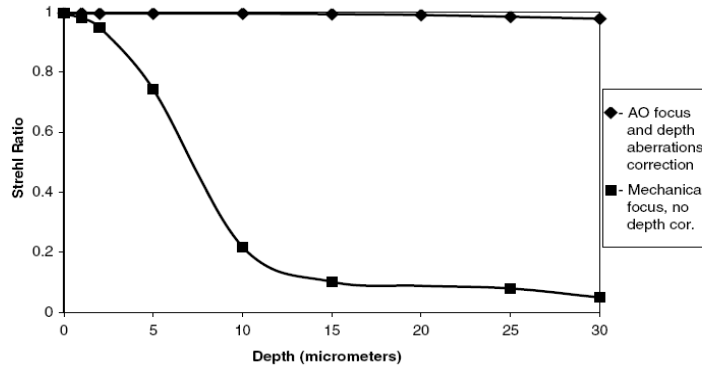


Figure 3.1: Strehl ratio comparison performed by Kam et al. [13]

An Adaptive Wide-Field Fluorescence system which directly measures wavefront aberrations with a Shack-Hartmann Sensor has shown improvement in the PSF of fluorescent microbeads injected into *Drosophila* embryos [7]. Fluorescent microbeads were used as the point source for the SHWFS in both of these systems. This system demonstrated an average two-fold increase in the Strehl ratio, with as much as a ten-fold improvement at a sample depth of 100 μ m. The improvement of the PSF and Strehl Ratio for a 1 μ m diameter microbead injected into the sample is shown in Figure 3.2.

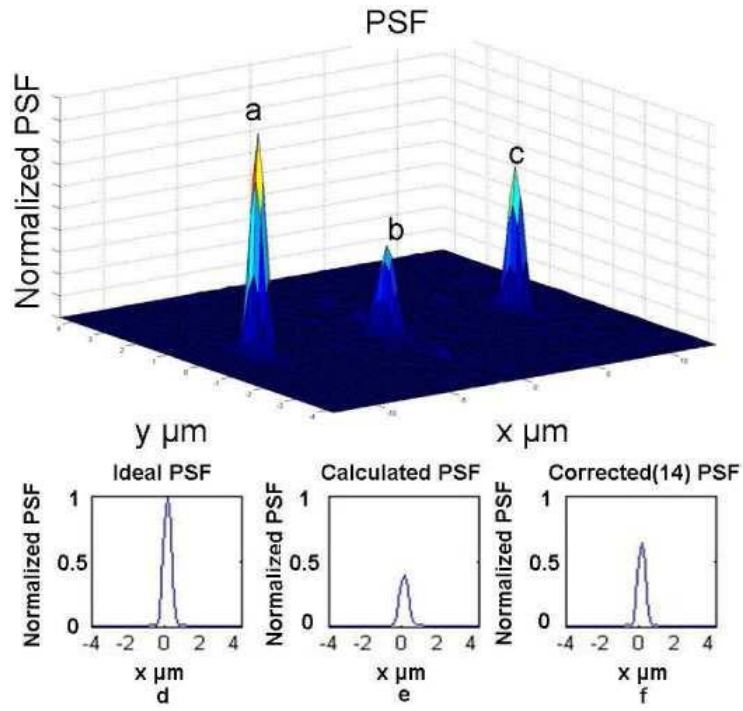


Figure 3.2: Results obtained by Azucena et al. showing improvement of the PSF and Strehl ratio
a) Ideal PSF b) Uncorrected PSF c) Corrected PSF [7].

CHAPTER 4

OBJECTIVES

Adaptive Optics has proven to be an effective means of improving image quality in astronomy [1] as well as confocal [3,30], multi-photon[4,5,19], and wide-field fluorescence microscopy [6,7]. The objective of this study is to develop a Shack-Hartmann wavefront sensor based Adaptive Optics system for a wide-field fluorescence microscope. We demonstrate the measurement wavefront aberrations caused by *C. elegans* using microbeads fixed beneath the sample as well as Green Fluorescent Protein (GFP) as the "guide stars" of the Adaptive Optics system. The following steps were taken to complete this objective:

- 1) Design and build a Shack-Hartmann Wavefront Sensor
 - a. Optical Design of Shack-Hartmann Sensor
 - b. Implement reconstruction algorithm – reconstruct wavefront to an accuracy of $.006\mu\text{m}$ RMS, which corresponds to 1% of wavelength of light being used
 - c. Calibration using known defocus aberrations
- 2) Integrate Adaptive Optic components with existing fluorescence microscope
- 3) Testing of AO system
 - a. Correct wavefront to an RMS of $.066\mu\text{m}$ when compared to a perfectly flat wavefront under:
 - i. Defocus aberrations
 - ii. Depth aberrations
- 4) Measurement and correction of aberrations caused by *C. elegans* using microbeads fixed beneath the sample.
- 5) Measurement of aberrations caused by *C. elegans* using Green Fluorescent Protein (GFP)

CHAPTER 5

SHACK-HARTMANN SENSOR

Components and Optical Setup

The Shack-Hartmann Wavefront Sensor proposed in this paper consists of a lenslet array (Thorlabs MLA150-7AR), relay imaging optics (Thorlabs MAP105050-A) and CCD camera (Photometrics HQ2). Unlike commercially available sensors, the CCD used for the SHWFS in this study is thermoelectrically cooled. This helps to reduce the dark current of the CCD chip, which improves the sensitivity of the camera when operating at low light intensities. The lenslet array consists of 6.7mm focal length lenses on a 150 micron spacing that split the input optical signal into an array of spots. Due to the short focal length of the lenslet array and the fact that the CCD chip is located within the camera body, two 50mm lenses are used to image the focal plane of the lenslet array onto the CCD chip. The optical setup of the Shack-Hartmann sensor is shown in Figure 5.1, with an image of the sensor in Figure 5.2.

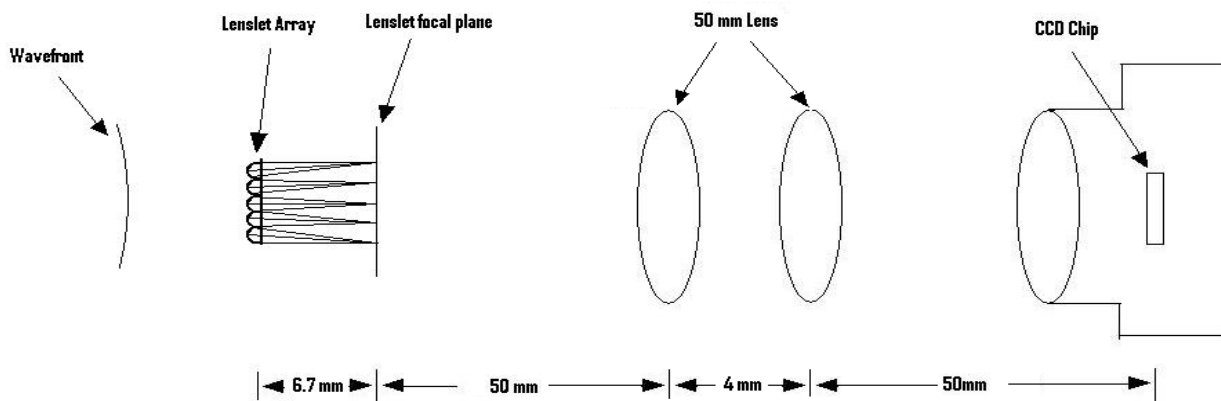


Figure 5.1: Optical setup of Shack-Hartmann Sensor

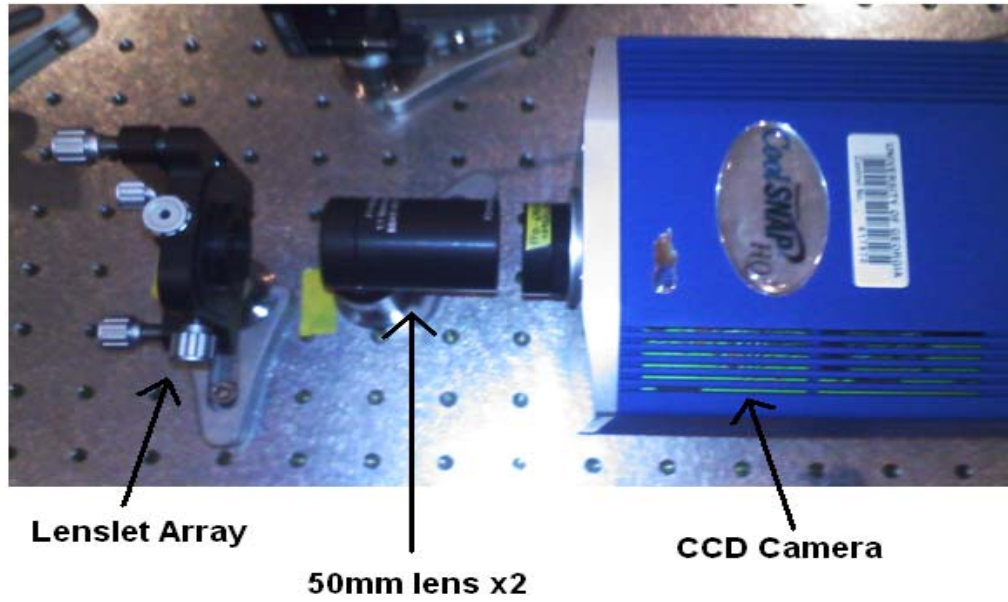


Figure 5.2: Shack-Hartmann Sensor

Sensor Signal

Crimson fluorescent microbeads (Invitrogen F8816) act as the point source for the sensor and are excited by a laser (Thorlabs S1FC635) focused to a confocal spot at the sample plane. The microbeads are $1\mu\text{m}$ in diameter, and the emission/excitation spectrum is shown in Figure 5.3. The excitation laser operates at 2.5 mW at a wavelength of 635 nm. This power output and the high photon density of the focused beam provide a suitable Signal to Noise ratio for shorter exposure times. A dichroic mirror is used to separate the excitation laser from much weaker fluorescence signal. A Shack Hartmann image with a max signal to noise ratio of 35 can be obtained with a 30ms exposure. Using a confocal spot as the excitation source for the Shack-Hartmann sensor signal ensures the wavefront is being measured from a single bead.

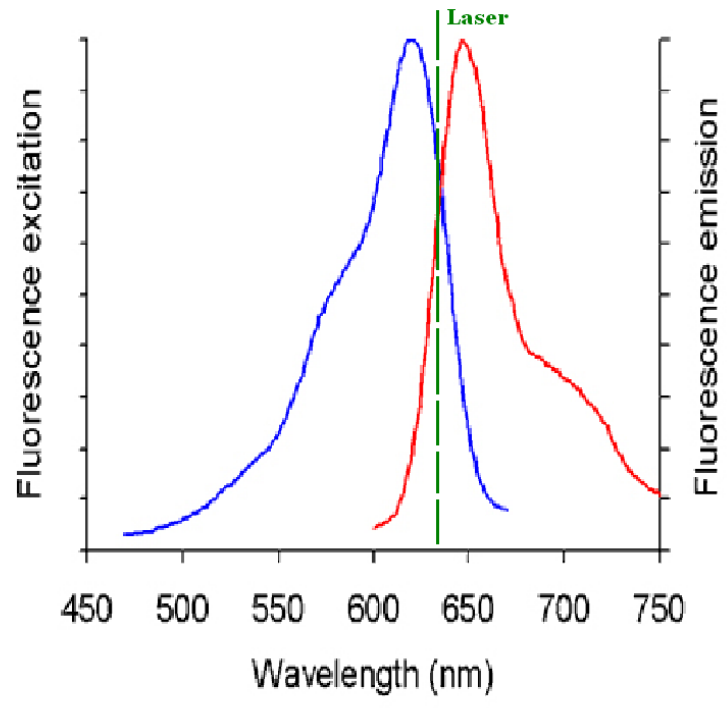


Figure 5.3: Excitation (blue) and emission (red) wavelengths for the Invitrogen F8816 microbeads

CHAPTER 6

WAVEFRONT CALCULATION

Gradient Calculation

The first step in calculating the wavefront is determining the shift of each Shack-Hartmann spot. To do this, the location of each spot when no aberration is present must first be determined. The excitation laser is focused on a bead fixed to the coverslip and a Shack-Hartmann image is obtained. This image represents the unaberrated Shack Hartmann spot locations and will be referred to as the baseline image. Preprocessing of all Shack-Hartmann images involves subtracting the background out of the image, then applying a threshold so that only the Shack-Hartmann spots remain. To estimate the background level, the average of a 50x50 pixel area outside of the aperture is determined. A simple searching algorithm iterates through the image and records a single pixel location for each Shack-Hartmann spot, and these locations are stored in an array. Each spot location is then considered the center of a 15x15pixel sub-aperture and a centroid calculation is performed. By calculating the centroid, the center for each Shack-Hartmann spot can be determined at sub-pixel resolution.

After determining the centroid for each Shack-Hartmann spot in the baseline image, a second Shack-Hartmann image is obtained by focusing onto a bead whose fluorescence travels through the aberrating medium that is being measured. This image will be referred to as the offset image. Using the sub-aperture locations determined in the baseline image, the centroid locations are calculated for the offset image. The distance between centroids of the baseline and

offset images in the x and y directions is recorded separately. These values are the x & y components of the wavefront shift over each sub-aperture in units of pixels.

The distances between the baseline and offset Shack-Hartmann spots must be converted into unit gradient values in units of microns. The relationship between the pixel difference and wavefront phase is shown in Figure 6.1. The wavefront phase (Φ) is related to the pixel shift (g) by Equation 6.1. In this equation, L refers to the pixel width of the CCD detector and f represents the focal length of the lenslet array. The gradient of the wavefront ($\Delta\theta$) is related to the wavefront phase by the pitch of the lenslet array (P). For the Thorlabs MLA150-7AR: $P = 150 \mu\text{m}$, $f = 6.7 \text{ mm}$, and $L = .00645 \text{ mm}$ for the Photometrics HQ2 camera. Using Equations 6.1 and 6.2, the pixel shift is converted to the change in the wavefront over the sub-aperture in units of microns.

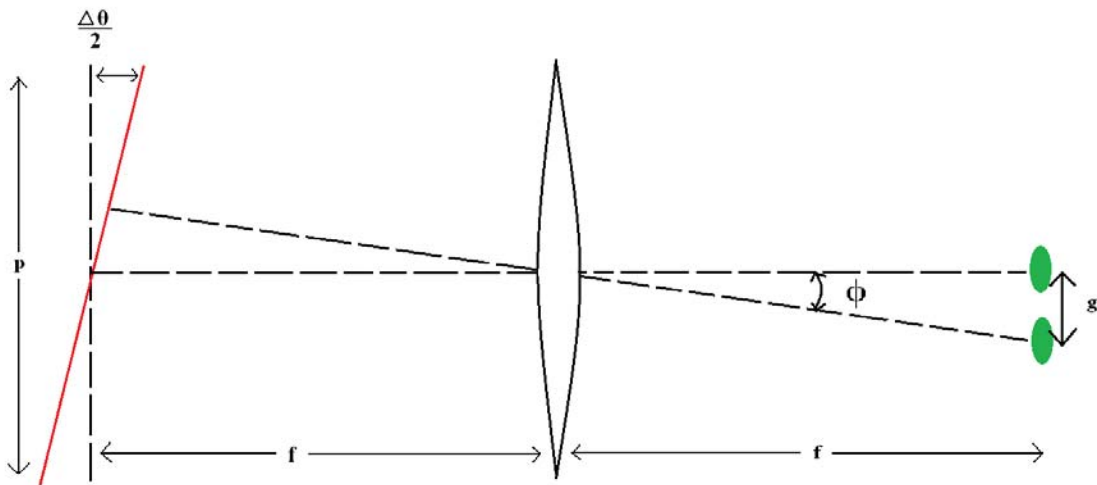


Figure 6.1: Relationship between pixel difference (g) and wavefront gradient (θ). Where Φ represents the wavefront phase and f is the focal length of the lenslet array.

$$\Phi = (gL/f) \quad \text{Eq. (6.1)}$$

Where: L = length of pixels, f = Lenslet array focal length, g = shift in Shack-Hartmann spots in pixels

$$\Delta\theta = P\Phi \quad \text{Eq. (6.2)}$$

Where: $\Delta\theta$ = wavefront gradient [μm], P = lenslet array pitch, and Φ = wavefront phase

Sorting Algorithm

After calculating the gradient corresponding to each Shack-Hartmann spot, the measurements must be placed in the same relative positions so that they each correspond to the correct lens of the lenslet array. A custom sorting algorithm is utilized to arrange the wavefront measurements. The algorithm first estimates the location of the center spot by finding the Shack Hartmann spots closest to the top, bottom, left, and right edges. The center spot location is estimated by finding the average of the top and bottom edges for the y-coordinate and the x-coordinate by averaging the left and right edge location. The estimated location of the center spot is then compared to the array of spot locations with the closest spot location to the estimated center becoming the central spot. The central spot is then placed into the center of a 50x50 array which holds the resulting wavefront measurement.

After determining the central spot, the algorithm sorts the spot locations array and orders the spot locations according to Figure 6.3. The algorithm starts with location zero, which is the central spot, and searches for other Shack-Hartmann spots along its horizontal plane. The algorithm then searches for a Shack-Hartmann spot directly above the current horizontal location in the same vertical plane as the central spot. If a spot location is found, the algorithm once again searches the horizontal plane for more Shack-Hartmann spots. After finding the spot

locations on the upper half of the aperture, the algorithm searches for a Shack-Hartmann spot directly below the center spot and proceeds to find the Shack-Hartmann spots in the same manner as before, but downwards. Spot locations are placed into a sorted array where their position in the array corresponds to the pixel value to a placement mask, an example of which is shown in Figure 6.4.

				54	52	53				
			51	50	47	48	49			
		46	45	44	40	41	42	43		
	39	38	37	36	31	32	33	34	35	
	30	29	28	27	22	23	24	25	26	
21	20	19	18	17	11	12	13	14	15	16
10	9	8	7	6	0	1	2	3	4	5
65	64	63	62	61	55	56	57	58	59	60
	74	73	72	71	66	67	68	69	70	
	83	82	81	80	75	76	77	78	79	
		90	89	88	84	85	86	87		
			95	94	91	92	93			
				98	96	97				

Figure 6.3: Sorting algorithm order

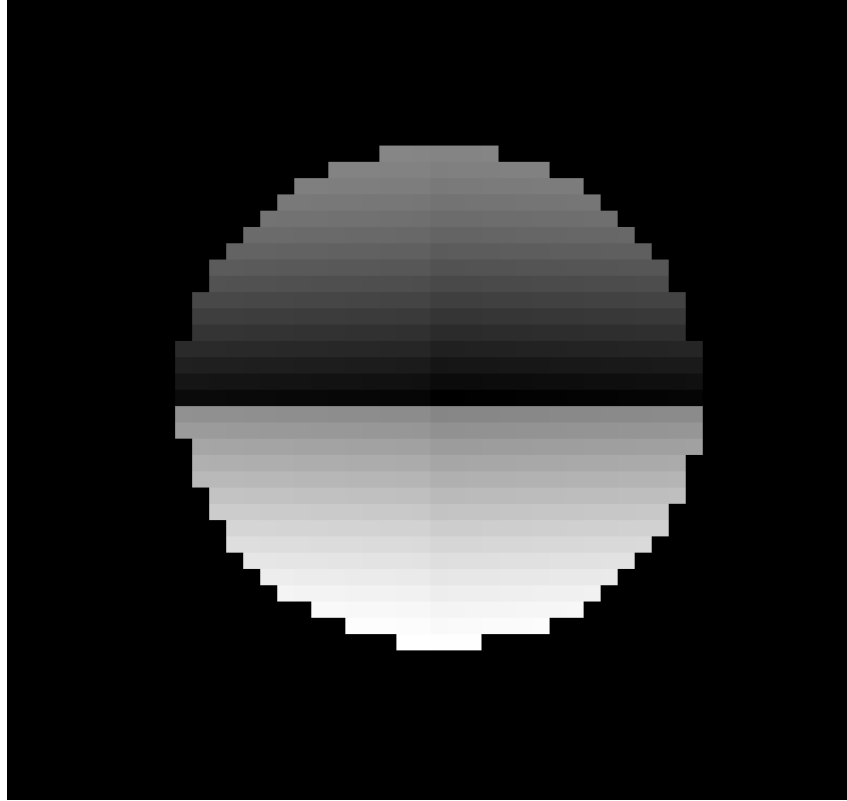


Figure 6.4: Placement mask for sorting algorithm: pixel value at each measurement point corresponds to the location of each sub-aperture center in the array of ordered locations

Wavefront Reconstruction

Simply put, the primary problem involves determining the wavefront from gradient measurements, which are susceptible to noise. A comprehensive review of the history of this problem, as well as a discussion of their numerical methods, is presented by Luke [31].

Output signals from SHWFS are proportional to the wavefront slopes [23]. The wavefront can be represented as an array of equally spaced nodes. The geometry of the sub-apertures containing the local gradient measurements affects the solution for the wavefront phase [11]. Fried proposed an orientation in which the measured gradients are located in the center of each sub-aperture, and the points of the wavefront to be calculated were located in the corners of these square sub-apertures (Figure 6.5). The measured gradients represent the first difference of

the wavefront nodes as described in Equation 6.3. Fried determined that this geometry resulted in wavefront reconstruction with very low residual mean squared error [32].

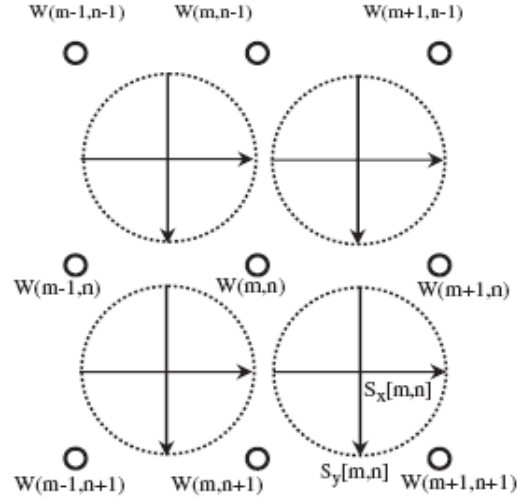


Figure 6.5: Fried Geometry: W = Wavefront, S_x, S_y = Gradients [33]

$$\begin{aligned} S_x[m,n] &= \frac{1}{2}(w[m, n+1] - w[m,n] + w[m+1,n+1] - w[m,n+1]) \\ S_y[m,n] &= \frac{1}{2}(w[m+1, n] - w[m,n] + w[m+1,n+1] - w[m+1,n]) \end{aligned} \quad \text{Eq. (6.3)}$$

Where: m, n = sub-aperture coordinates

Several reconstruction methods have been developed for determining the wavefront from gradient measurements. By representing the relationship between the gradients and wavefront nodes as a system of linear equations according to Equation 6.4, the wavefront can be determined through matrix operations. This equation can be solved by Gaussian methods, which involve multiplying each side of the equation by the transpose of matrix A and then inverting the resulting square matrix [1]. Another solution utilizing matrices forces the resulting wavefront to

have a mean value of zero [34]. This is accomplished by extending the A matrix with an extra row of 1's and adding an extra zero to the gradient vector.

$$\hat{s} = Aw + n \quad \text{Eq. (6.4)}$$

Where: \hat{s} = vector of gradient measurements, A = matrix depending on the geometry of the gradients and wavefront nodes, w = vector of wavefront nodes, and n = noise.

Reconstructing the wavefront using matrix operations is sufficient for corrective devices with small numbers of actuators. However, the number of numerical operations greatly increases with more actuators, increasing computation time. The use of the Fourier Transform in determining the wavefront from gradient measurements has proven successful in large Adaptive Optics systems [35]. The shift property of the Fourier transform can be used to solve Equation 6.3 for the wavefront (w). Applying the Discrete Fourier Transform to Equation 6.3 results in Equation 6.5. Rearranging this equation to solve for w gives the relationship between the gradients and wavefront as shown in Equation 6.6. Taking the inverse Fourier Transform of w in Equation 6.6 gives the estimated wavefront. Numerous numerical algorithms and methods have been developed that result in quality estimations of the wavefront [33,35,36]. The algorithm used in our system was developed by Dr. Huanquin Guo and Dr. Zhaoqi Wang [33].

$$\begin{aligned} DFT\{S_x\} &= \frac{1}{2}w(k, l) \left\{ \exp\left[\frac{i2(k+l)\pi}{N}\right] + \exp\left(\frac{i2k\pi}{N}\right) - \exp\left(\frac{i2l\pi}{N}\right) - 1 \right\} \\ DFT\{S_y\} &= \frac{1}{2}w(k, l) \left\{ \exp\left[\frac{i2(k+l)\pi}{N}\right] + \exp\left(\frac{i2l\pi}{N}\right) - \exp\left(\frac{i2k\pi}{N}\right) - 1 \right\} \end{aligned} \quad \text{Eq. (6.5)}$$

Where: k, l = coordinates in spatial frequency domain, N = grid size

$$w(k, l) = \begin{cases} 0, k = l = 0, k = l = N/2 \\ \left\{ \left[\exp\left(-\frac{i2k\pi}{N}\right) - 1 \right] \left[\exp\left(-\frac{i2l\pi}{N}\right) + 1 \right] DFT\{S_x\} \right. \\ \left. + \left[\exp\left(-\frac{i2l\pi}{N}\right) - 1 \right] \left[\exp\left(-\frac{i2k\pi}{N}\right) + 1 \right] DFT\{S_y\} \right\} \\ \times \left[8\left(\sin^2\frac{k\pi}{N}\cos^2\frac{l\pi}{N} + \sin^2\frac{l\pi}{N}\cos^2\frac{k\pi}{N}\right) \right]^{-1} \end{cases} \quad \text{Eq. (6.6)}$$

Based on the work accomplished by Fried as well as work by Freischland and Koliopoulos, who first proposed the use of Fourier transforms in wavefront estimation [37], Dr. Guo and Dr. Wang developed a new iterative algorithm to estimate the wavefront of a system based on noisy gradient measurements. This method was proven to produce estimations of the wavefront that were more accurate than estimations based on Zernike expansion polynomials or other reconstructions such as the Roddier-Gerchberg algorithms [33].

Because the wavefront gradients are not measured accurately across the edge of the wavefront, errors occur across the aperture boundary of the image. The reconstruction algorithm solves this problem by iteratively improving the wavefront estimate. The wavefront is first estimated using Equation 6.2, with all gradients outside the aperture set to zero [33]. The gradients are then recalculated based on Equation 6.3, which is based on the Fried Geometry [38]. The re-calculated gradients located outside of the aperture are then placed into the original gradient matrices and the wavefront is once again estimated.

The Shack-Hartmann sensor shows little or no response to certain aberration modes [39]. The most common of these for the Fried Geometry is Waffle mode, which is due to the fact that disjointed gradients in the x and y directions must be recombined to calculate the wavefront. Waffle mode is basically a repeated astigmatic pattern over the entire aperture at the same frequency as the Shack-Hartmann sensor sampling. Waffle error manifests itself as a checkerboard-like pattern as shown in Figure 6.7. An additional waffle removal step, developed

by Poyneer et al., was added to the algorithm to remove the global waffle error [35]. A constant is determined using Equation 6.7, where w represents the wavefront, v represents the waffle mode, and m, n are coordinates. The constant is then multiplied by v and subtracted from the wavefront, removing the global waffle error.

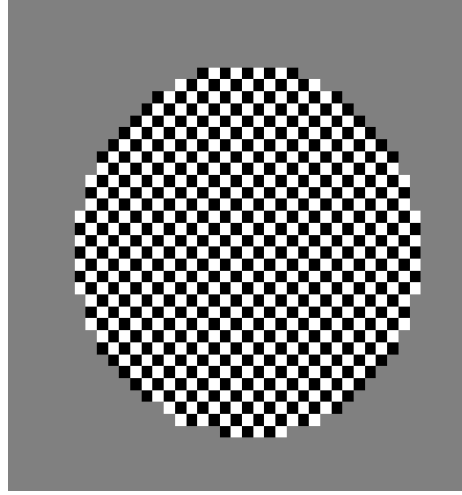


Figure 6.6 – Waffle error caused by recombining the disjointed x and y gradients to calculate the wavefront

$$C_v = \frac{\sum_{m=0}^{N-1} \sum_{n=0}^{N-1} w[m,n]v[m,n]}{\sum_{m=0}^{N-1} \sum_{n=0}^{N-1} v[m,n]v[m,n]} \quad \text{Eq. (6.7)}$$

Where C_v is the Waffle mode constant, w is the wavefront, v is the aberation mode, and m,n are coordiantes [34].

Programming software

Priithon, a Python based image analysis platform was used to control the Adaptive Optics system. Additional add-on packages, developed specifically for Python (Scipy, Numpy), were utilized to perform array and centroid calculations. To control the Photometrics HQ2 camera,

deformable mirror, and microscope stages, it was necessary to use a foreign function library built for Python, which provided C compatible data types and a python interface to C libraries.

CHAPTER 7

DEFORMABLE MIRROR

Correction of measured wavefronts is accomplished using a Mirao-52e deformable mirror. This mirror consists of 52 electromagnetic actuators beneath a 15mm reflective surface. As mentioned previously, a 20 μ m stroke is required to correct depth aberration of around 100 μ m. Measurement of aberrations caused by *C. elegans* (discussed in Chapter 10) show that the magnitude of aberration is well within the capabilities of the deformable mirror. The Mirao-52e deformable mirror is capable of a $\pm 35\mu$ m stroke for Defocus aberrations and $\pm 30\mu$ m stroke for Astigmatism.

The actuator voltages can be related to the mirror shape by measuring the wavefront for different actuator commands using Equation 7.1 [7]. The wavefront is a 50x50 image with an aperture diameter of 31 pixels centered at position 25,25. The influence function array H gives the relationship between the actuator voltages for each piston and the wavefront. This array is determined by applying a set voltage to each piston individually and measuring the resulting wavefronts. Figure 7.1 shows the resulting wavefront caused by applying a set voltage to a single actuator.

$$H * A = W \qquad \text{Eq. (7.1)}$$

Where H = Influence function array, A = Actuator voltages array, W = wavefront

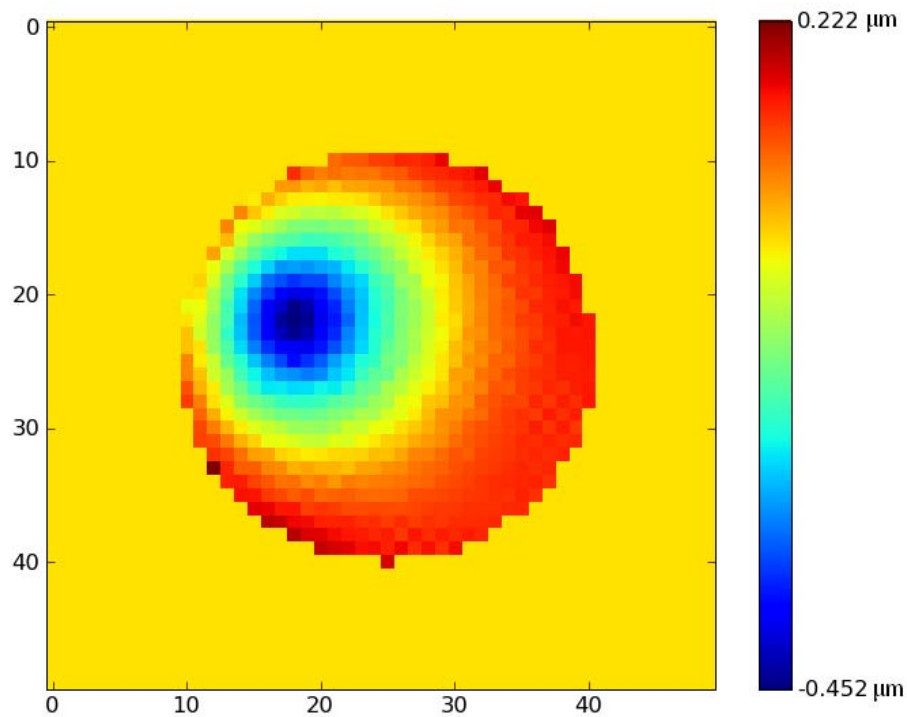


Figure 7.1: Influence function example

The influence functions can be arranged into a 2500×52 matrix where each column holds the wavefront corresponding to an actuator where each wavefront is reshaped from a 50×50 array to a 2500×1 vector. To determine the mirror settings, Equation 7.1 must be solved for A , which requires determining the inverse of the influence function array H . The inverse of the influence function is calculated using singular value decomposition. Matrix multiplication of the inverse influence function and measured wavefront results in a 52×1 vector of actuator voltages, which are used to set the deformable mirror.

Chapter 8

SHACK-HARTMANN SENSOR CALIBRATION

Wavefront reconstruction algorithm testing

The preliminary experiments involved calibration of the wavefront sensor. To test the accuracy of the algorithm, the first nine Zernike polynomials were reconstructed from simulated wavefront gradient data and a root mean square error analysis was performed. Each Zernike mode was scaled to have an amplitude of 2 microns. The calculation of the gradients from the known wavefront is discussed in Chapter 4.

The RMS errors for the first nine Zernike Modes are shown in Figures 8.1 and 8.2. The RMS errors in reconstructing the 3rd and 8th Zernike polynomials are shown separately due to their magnitude. In all cases, the goal of reconstructing the wavefront within 1% of the wavelength of light being used is achieved. The results show that an accurate reconstruction of the wavefront is achieved using the previously described algorithm by Guo and Wang [33]. An example of the original and reconstructed wavefront for the 4th Zernike polynomial is shown in Figure 8.3.

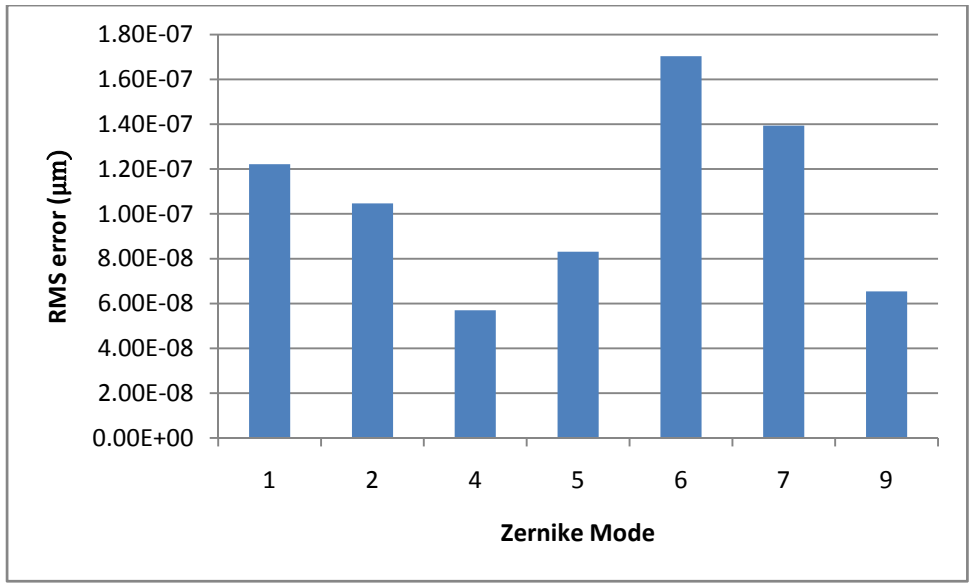


Figure 8.1: RMS error for several reconstructed Zernike Polynomials at amplitudes of 2μm.

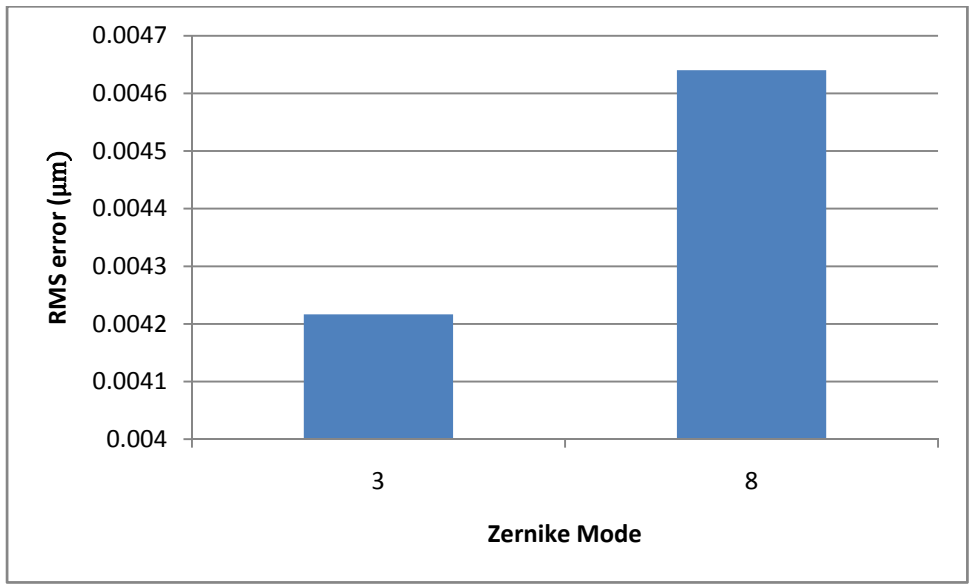
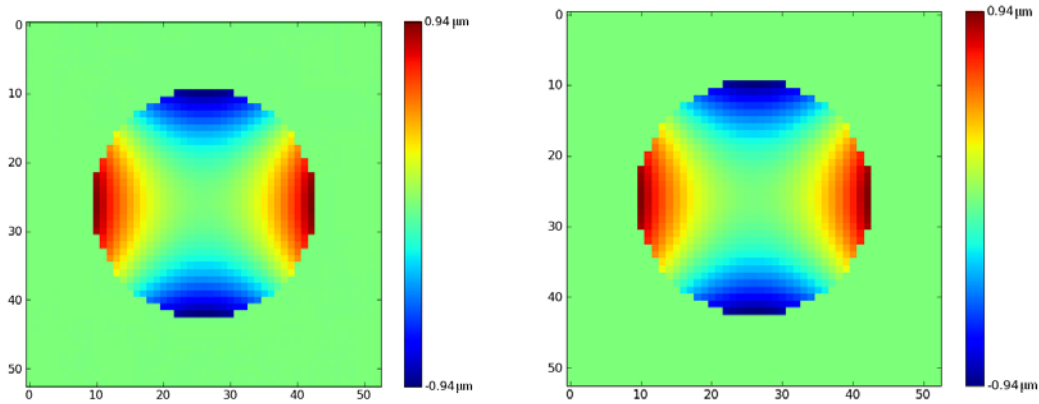


Figure 8.2: RMS error for 3rd and 8th Zernike Modes at amplitudes of 2μm.



a) b)
Figure 8.3: Starting (a) and Reconstructed (b) wavefronts for the 4th Zernike Polynomial.

Optical alignment Calibration

Initial placements of the optical elements of the Shack-Hartmann sensor were based on physical measurement of distances. The fiber laser was mounted to the microscope and used to fine tune the optical alignment. Aligning the reflections of the laser off of each surface of an optical element ensured that the beam path traversed through the center of each component and that the component was normal to the beam. Further calibration of the optical alignment and setup of the SHWFS was accomplished by comparison of defocus aberrations to theory [6,19].

Initial calibration of the Shack-Hartmann sensor was accomplished using a single 1 μm diameter Yellow-Green fluorescent microsphere (Invitrogen F8811) excited by Thorlabs M470L1 LED and fixed to a cover-slip. Wavefront measurements were taken using the focused bead as the baseline Shack-Hartmann image, and moving the z-stage of the microscope (Prior NanoScan Z) by a certain distance to obtain the offset Shack-Hartmann image. Figure 8.4 displays how the spots from the offset Shack-Hartmann image (red) are shifted by 5 microns of defocus from their original locations in the baseline image (green). Slides were prepared by

drying 15 microliters of microbead solution at a dilution of $1e^{-6}$ from the original concentration (2% by weight). Low concentrations of microbeads were necessary so that only one microbead would be within the field of view. The aberrations due to focus from $-5\mu\text{m}$ to $5\mu\text{m}$ were calculated and compared to theory (Equation 8.1), and the results are displayed in Figures 8.5 - 8.8. The RMS errors are shown in Figures 8.9 and 8.10.

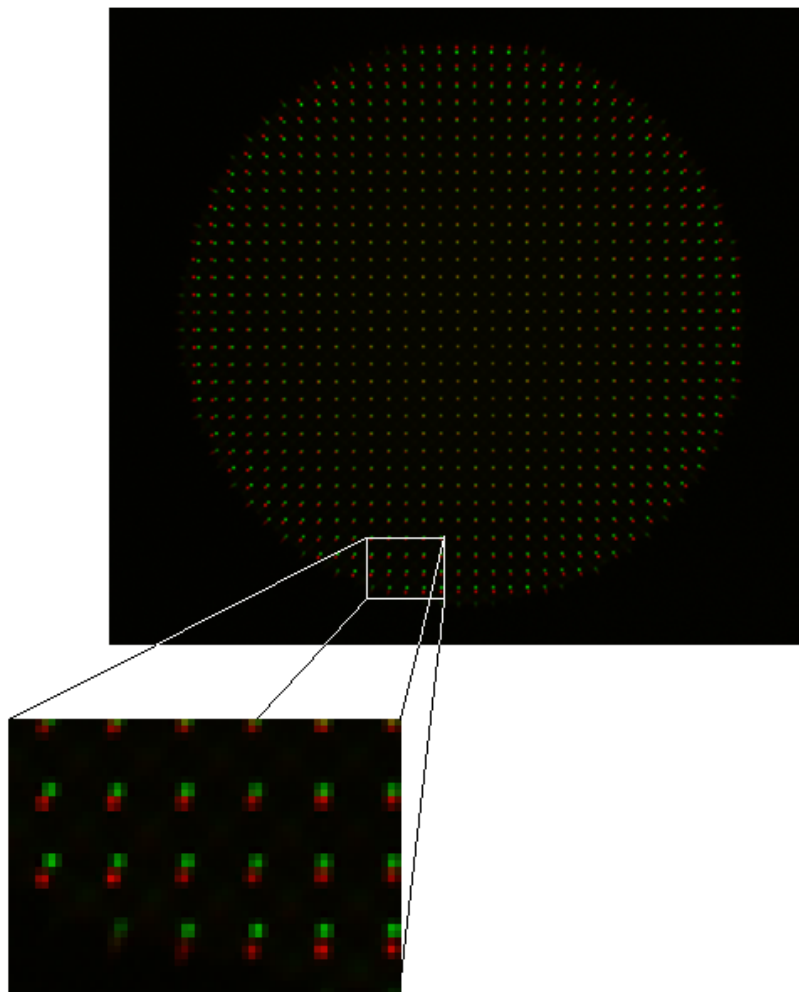


Figure 8.4: Shifting of Shack-Hartman spots in the baseline (green) and offset (red) Shack-Hartmann images due to 5 microns of defocus.

$$\varphi = n_2 d \sqrt{1 - \left(\frac{NA\rho}{n_2}\right)^2} \quad \text{Eqn. 8.1}$$

Where: φ = aberration, NA = Numerical aperture of optical system, n_2 = refractive index of immersion medium, d = depth, ρ = normalized radial coordinate

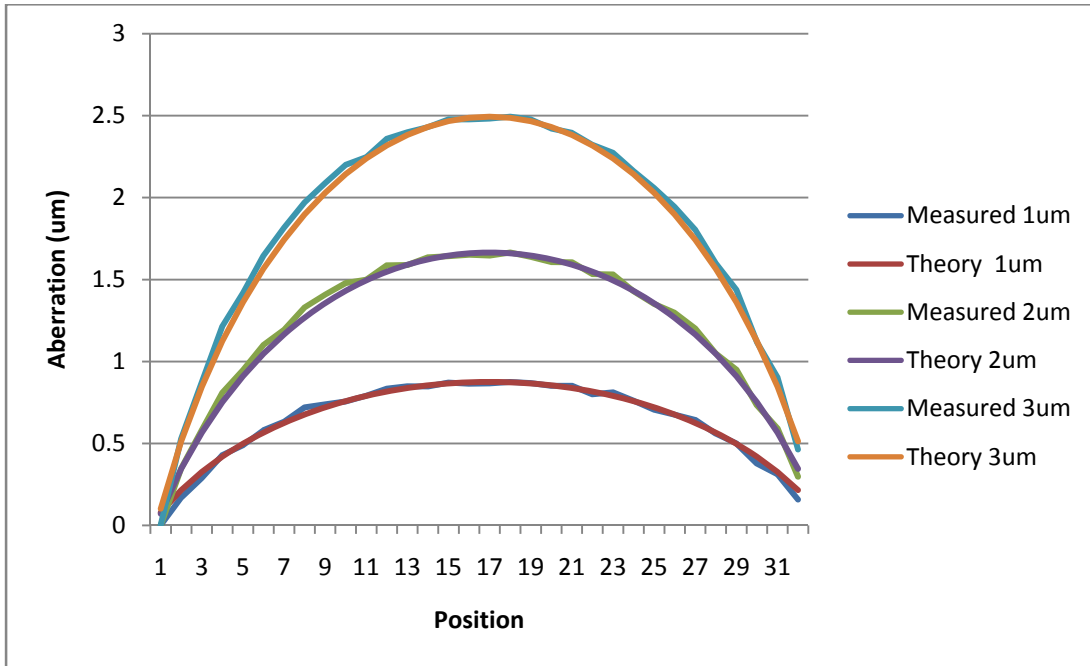


Figure 8.5: Theoretical and Measured Defocus Aberrations 1-3 microns

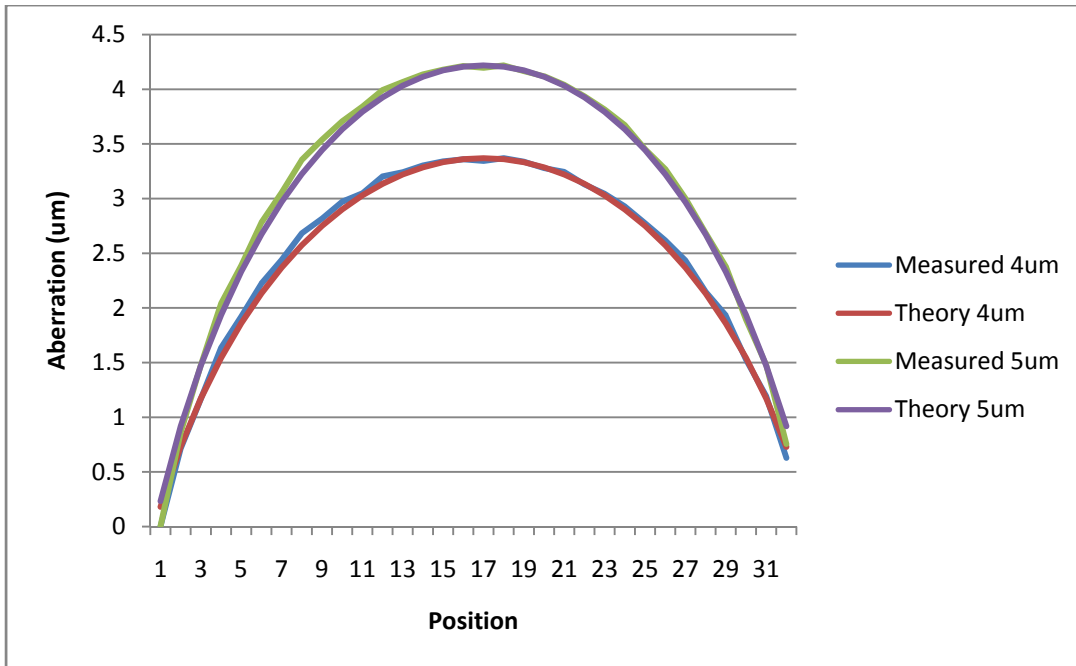


Figure 8.6: Theoretical and Measured Defocus Aberrations 4-5 microns

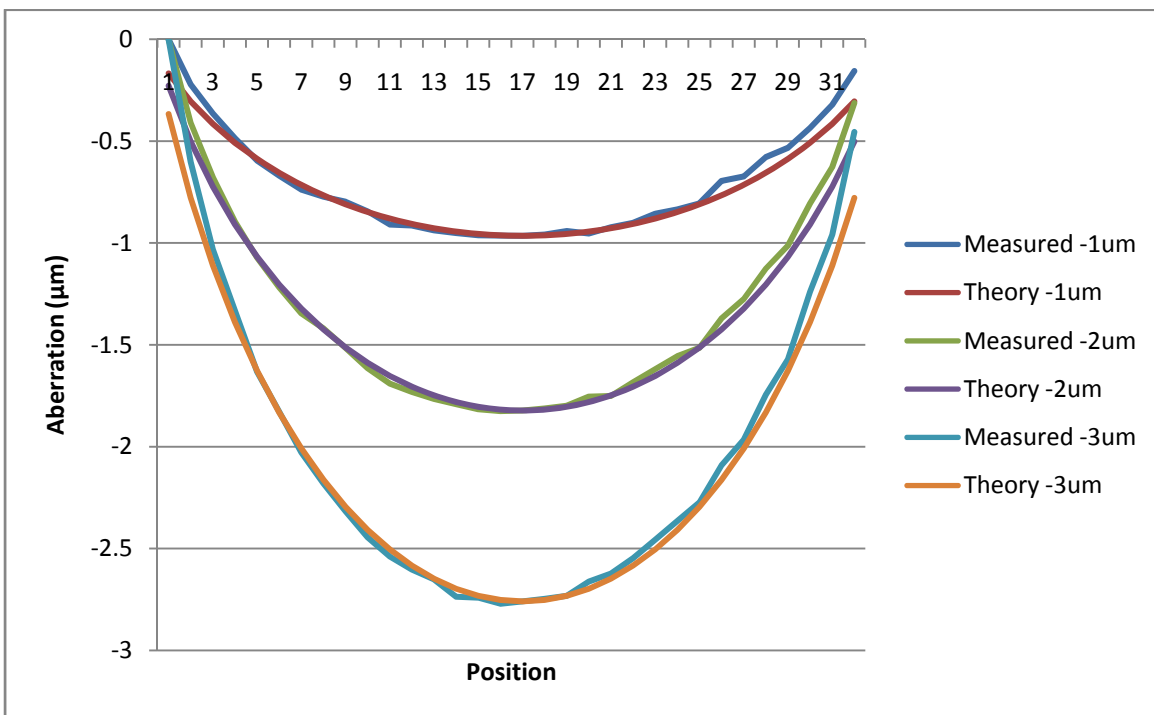


Figure 8.7: Theoretical and Measured Defocus Aberrations -1 to -3 microns

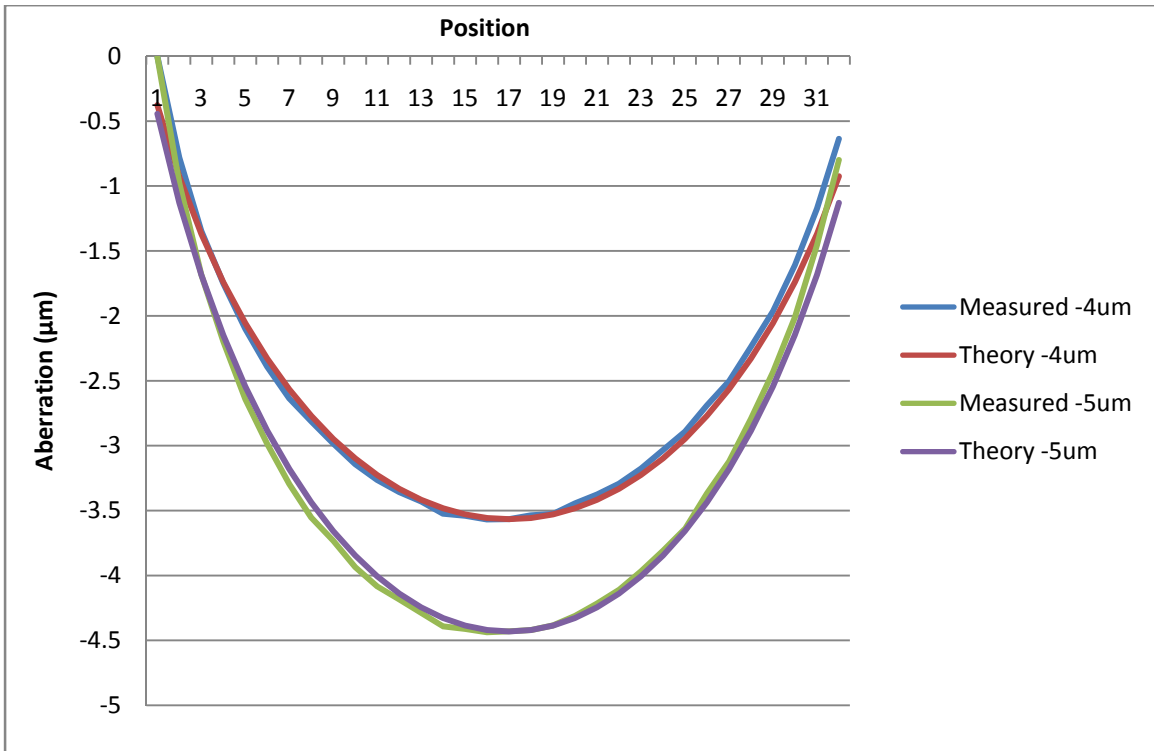


Figure 8.8: Theoretical and Measured Defocus Aberrations -4 to -5 microns

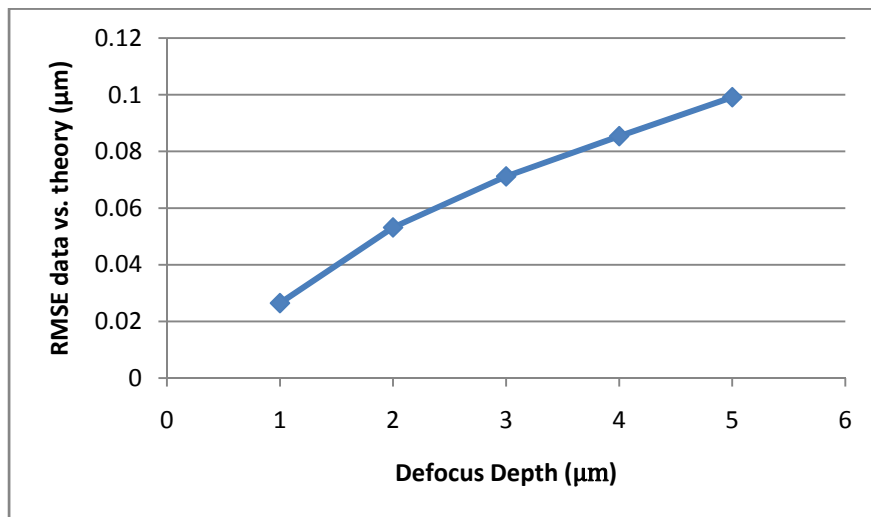


Figure 8.9: RMS errors of measured vs. theoretical defocus aberrations from 1 to 5 microns defocus

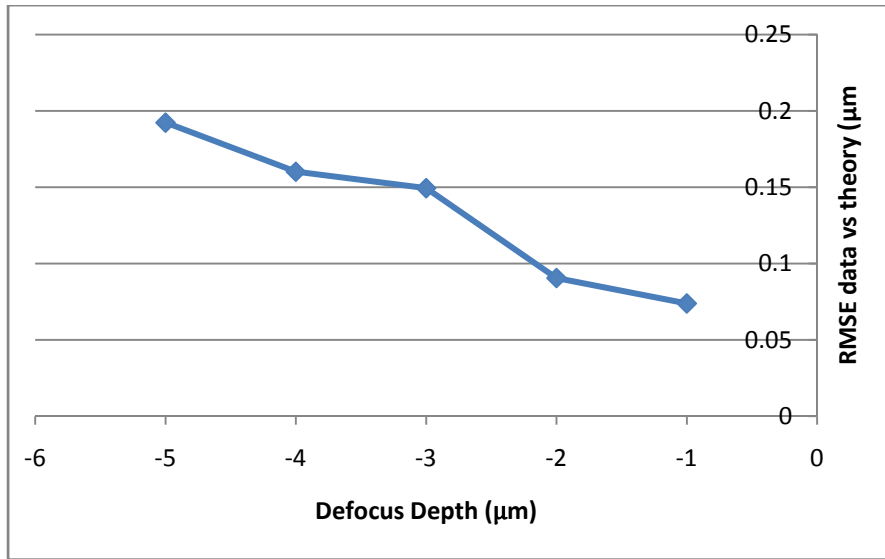


Figure 8.10: RMS errors of measured vs. theoretical defocus aberrations from -1 to -5 microns of defocus

Chapter 9

Testing of the Adaptive Optics system

Adaptive Optics System Description

The components of the Adaptive Optics system are integrated with the fluorescence microscope according to Figure 9.1. The microscope utilized for this system is an Olympus IX71 with a PlanApo N 60x oil immersion objective. The Dichroic mirrors: D1, D2, and D3 are custom made by Omega Optical (495DCLP, 555DCLP, and 645DCLP). D1 is used to insert the Newport Cyan (488 nm) excitation laser into the system, which is used as the excitation source for GFP. D2 has a transmittance near zero between 510nm and 540nm allowing the Invitrogen F8811 YG microbeads and GFP to be imaged on the Andor camera. D3 separates the excitation laser for the Shack-Hartmann Sensor signal (Invitrogen F8816 crimson microbeads) from the excitation source (Thorlabs S1JC635 laser). This custom dichroic has a steep increase in transmittance around 650nm, reflecting the 635nm wavelength laser while transmitting the 660nm wavelength microbeads. The Thorlabs S1JC635 laser beam is focused at the microscope, while the cyan laser illuminates the entire field of view.

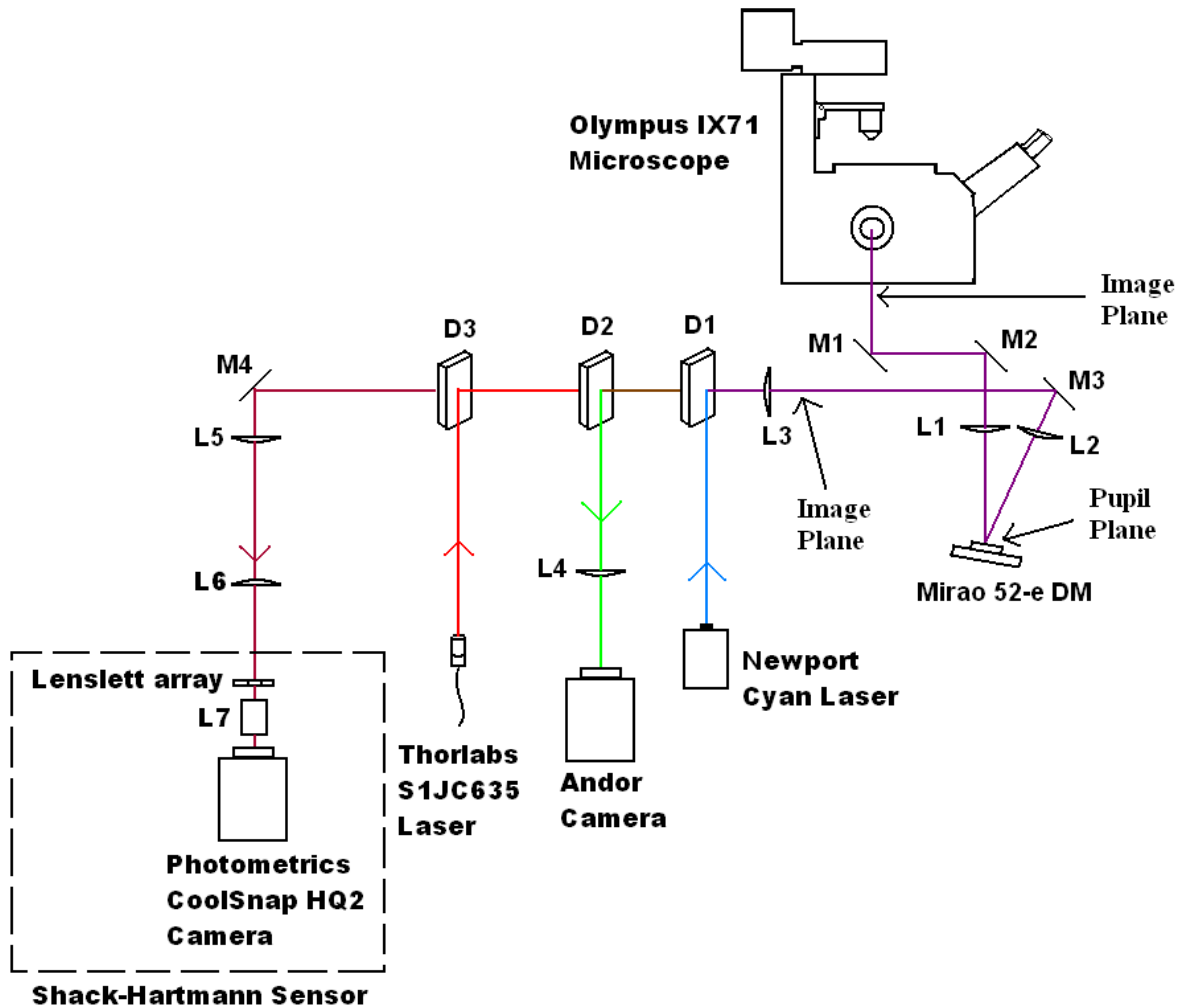


Figure 9.1: Adaptive Optics Fluorescent Microscope system

An image plane for the microscope exists 102 mm off of the microscopes side port. Lenses L1 and L2 have a 350mm focal length. L1 is used to reimagine the back-pupil plane on the Mirao 52-e deformable mirror. Lenses L3, L5, and L6 are used as relay optics where the focal length of L3 is 100mm and the focal lengths of both L5 and L6 are 300mm. L7 consists of the two 50mm lenses discussed in Chapter 5, which are needed due to the short focal length of the lenslet array. Mirrors M1 and M2 provide greater control of the excitation sources going into the

side port of the microscope and sample signal going into the Deformable Mirror. Mirror M3 is necessary due to the shape of the Optics table.

The numerical aperture of the system is limited to 1.28 by the deformable mirror diameter. For this reason, it was necessary to repeat the alignment using known defocus aberrations after the deformable mirror was inserted. The procedure for this experiment remained the same as discussed in Chapter 8. However, crimson beads excited by the single mode fiber laser were used. RMS errors comparable to the initial calibration were achieved. For example, an RMSE of $0.086\mu\text{m}$ was obtained for aberrations caused by $3\mu\text{m}$ of defocus.

Wavefront Correction Goals

Wavefront corrections were considered successful if the Root Mean Square (RMS) error when compared to a perfectly flat wavefront was less than $\lambda/10$. The Marechal criteria, which states that a system can be considered well corrected when the Strehl ratio exceeds 0.8 and corresponds to a wavefront error of less than $\lambda/14$. This criterion was originally developed for fixed optical systems and is overly restrictive for Adaptive Optics systems [1]. For this reason, the correction goal was reduced to a RMSE of less than $\lambda/10$. For the Invitrogen F8816 crimson microbeads, an RMSE of $.066\mu\text{m}$ when compared to a perfectly flat wavefront was considered successful.

To reach this goal, it was necessary to iteratively improve the actuator commands of the Deformable Mirror. During the initial wavefront measurement, the actuators are set to produce a flat surface. The voltages needed to accomplish a flat surface were established by a phase retrieval technique [40, 41]. Phase retrieval calculates the wavefront using three-dimensional wide-field images of fluorescent beads. Multiple images are taken around the focal plane and used to determine the phase of the wavefront in the back-pupil plane of the microscope objective. The

actuator settings corresponding to the measured wavefront were determined by solving Equation 7.1 for the actuator voltages array (A). The initial actuator voltages applied to the deformable produce a flat wavefront. The actuator voltages calculated by solving Equation 7.1 are subtracted from these initial commands to correct the measured aberrations. The correction is then applied and the wavefront is once again measured. As new actuator voltages are calculated, they are subtracted from the voltages of the previous measurement. Iterative correction continues until the RMS of the wavefront when compared to an array of zeros (a perfectly flat wavefront) reaches the correction goal. The equation for calculating the RMS error is shown as Equation 9.1.

$$\text{RMS} = \sqrt{(\sum(I_m - I_R)^2/n)} \quad \text{Eq. (9.1)}$$

Where: I_m = Measured Wavefront, I_R = Flat Wavefront, n = number of measurement points

Correction of Defocus Aberrations

The initial test of the Adaptive Optics involved the correction of 3 micron Defocus aberrations. Slides were prepared in the same manner as discussed in Chapter 8. The baseline Shack-Hartmann image was obtained from a microbead fixed to the coverlip. The Nanoscan Z stage was then moved by 3 μm , the offset Shack-Hartmann image obtained, and the wavefront measured. Final RMS errors of .068 μm for Trial 1 and .065 for Trial 2 when compared to a perfectly flat wavefront were achieved after ten iterative corrections. This represents a significant improvement to the RMS error for 3 μm of defocus which was calculated to be 0.67 μm . Figures 9.3 and 9.4 display the wavefronts before and after correction for each trial. All wavefront

figures have been color-mapped to improve clarity. Figures 9.5 and 9.6 display horizontal profiles across the diameter of the wavefronts before and after wavefront correction.

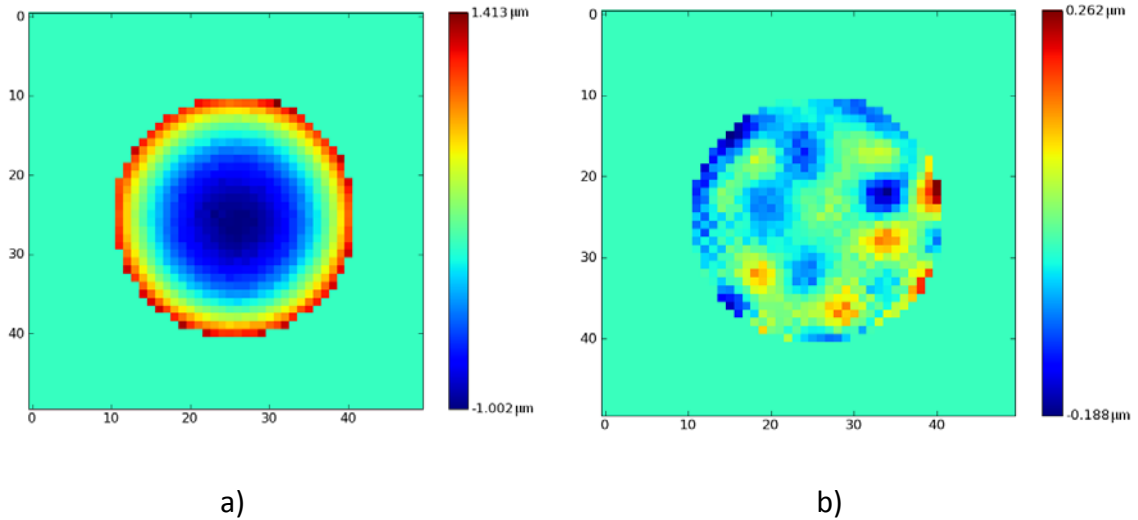


Figure 9.3: Aberrations due to 3 microns of defocus before (a) and after (b) correction for Trial 1

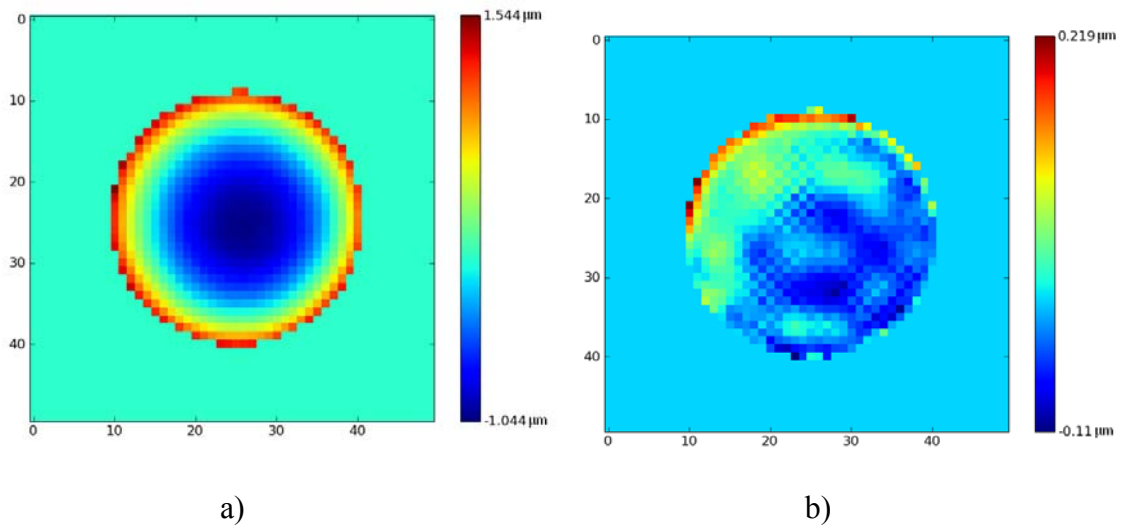


Figure 9.4: Aberrations due to 3 microns of defocus before (a) and after (b) correction for Trial 2

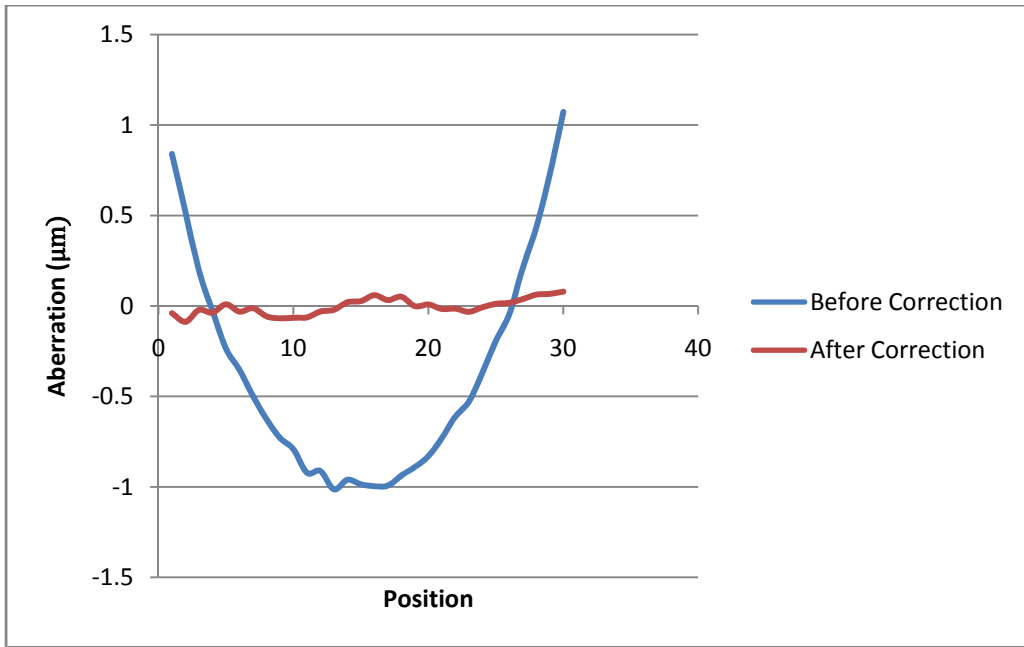


Figure 9.5: Horizontal profile of wavefront before and after correction of aberrations caused by 3 μm of defocus for Trial 1

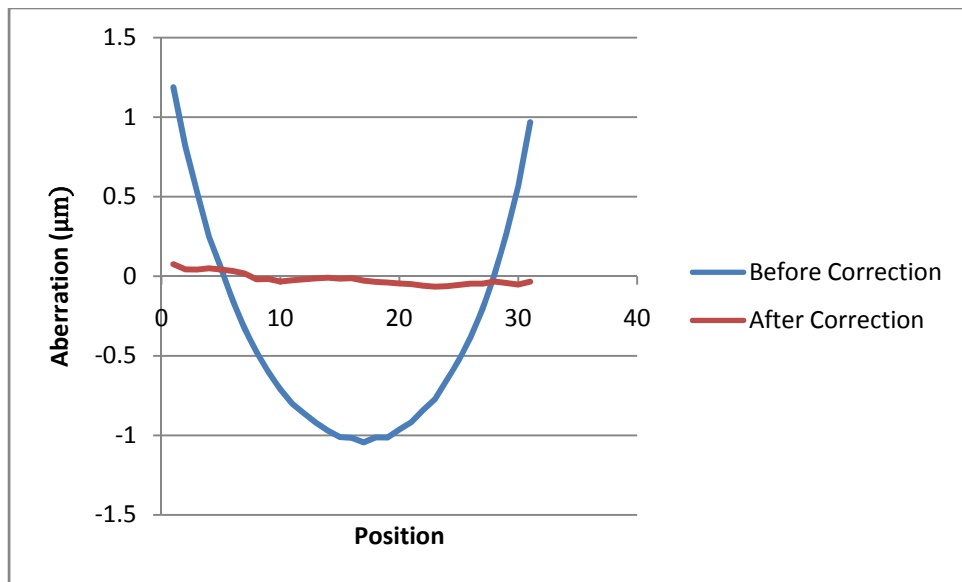


Figure 9.6: Horizontal profile of wavefront before and after correction of aberrations caused by 3 μm of defocus for Trial 2

Correction of Depth Aberrations

To further test the system, aberrations due to depth (Equation 2.6) were measured and corrected. Invitrogen F8816 crimson microbeads at a dilution of $1e^{-4}$ were fixed to both the coverslip and microscope slide and used to obtain the baseline and offset Shack-Hartmann images respectively. Thirty microliters of glycerol (index of refraction = 1.473) separated the coverslip and slide resulting in a depth of 37 microns. Figure 9.7 displays the wavefront before and after correction. Figure 9.7b has been up-scaled so that the wavefront is visible. A horizontal profile across the diameter of the wavefront before and after correction is shown in Figure 9.8. A final RMS error of $.054\mu\text{m}$ was achieved after seven iterative corrections, showing a reduction from the RMS error of the aberrated wavefront, which was calculated to be $.107\mu\text{m}$.

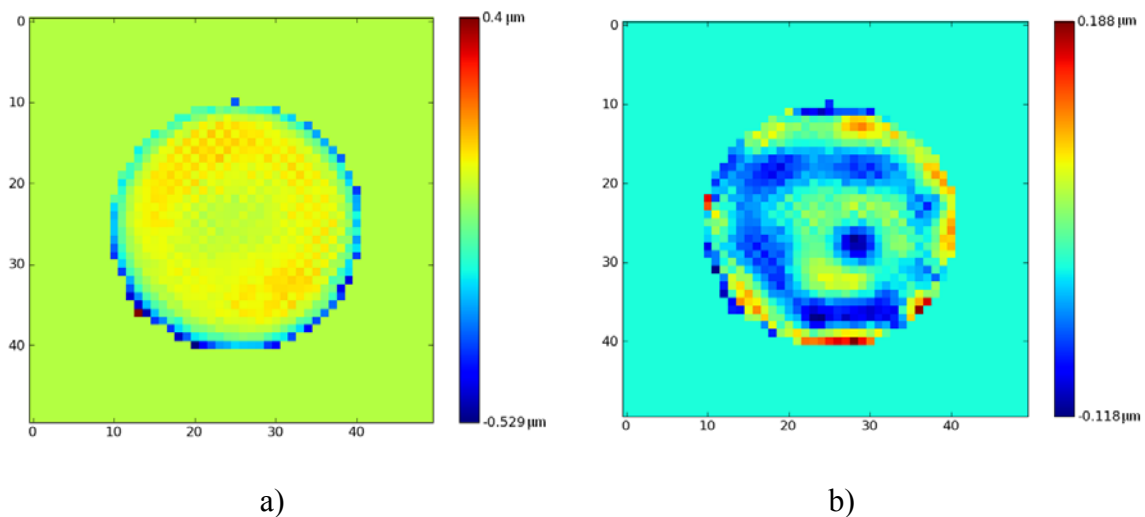


Figure 9.7: Aberrations due to depth in refractive index mismatch before(a) and after(b) correction.

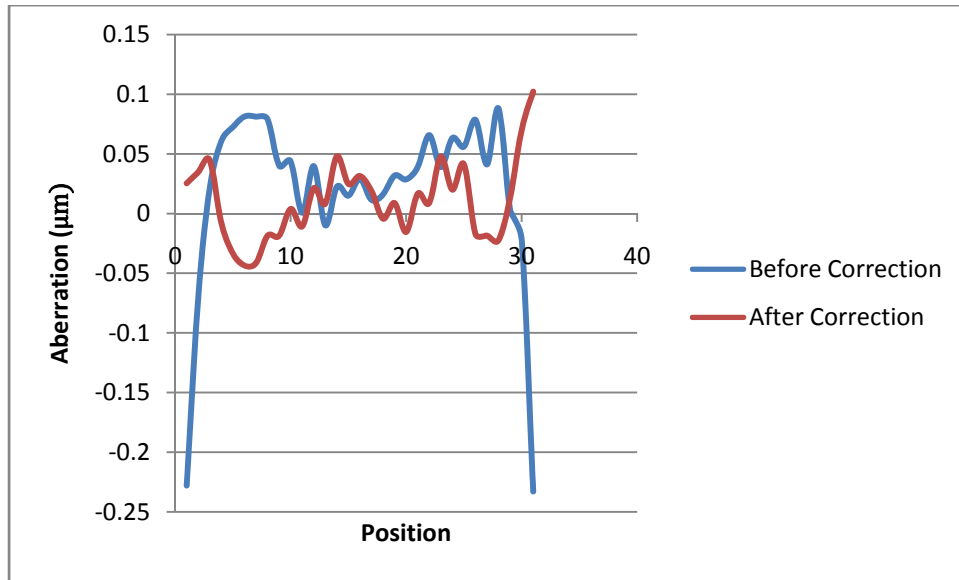


Figure 9.8: X-profile of aberrations caused by focusing into sample 37 μm before and after correction

Additional tilt/tip aberrations are a result of using separate beads for the baseline and offset Shack-Hartmann images. Due to the beam width of the excitation laser, an adequate signal can be achieved within a circular area with a diameter around 3 microns. Slight movement of the micro-bead will result in a shifting of all Shack-Hartmann spots. This shift is the cause of existing tilt in the horizontal profile in Figure 9.8.

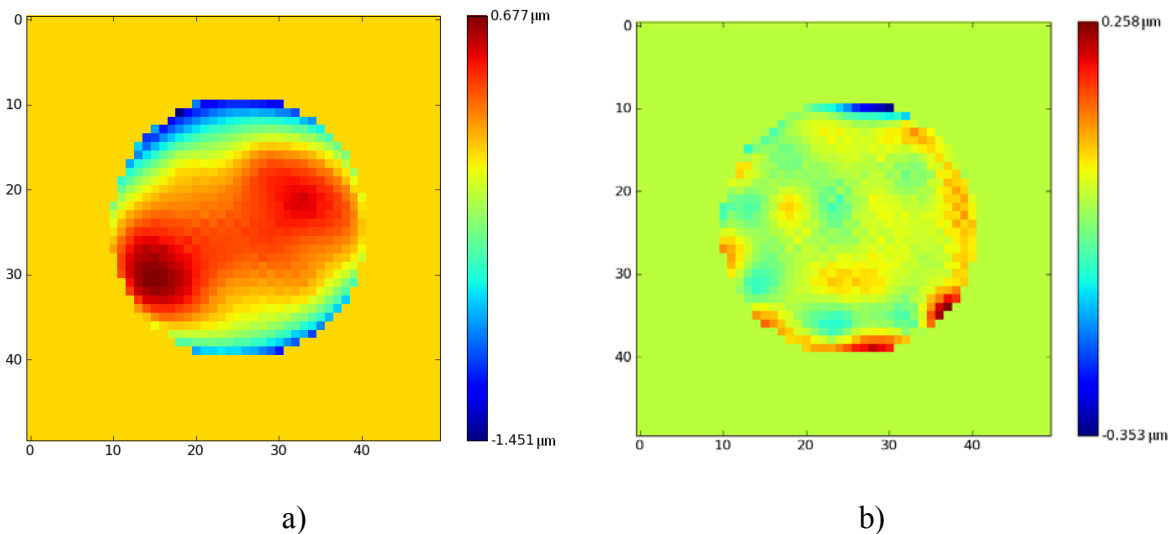
Correction of Induced Aberrations

To further test the Adaptive Optics system, and produce visual results, aberrations were induced through the deformable mirror and then corrected. To induce aberrations, all piston voltages were set to zero. Because the Mirao Deformable Mirror is not flat when all pistons are set to zero, aberrations are induced.

To calculate the wavefront, 1 μm crimson microbeads were fixed to the coverslip to obtain the baseline Shack-Hartmann image. A mixture of 0.2 μm yellow-green microbeads and 1 μm crimson beads at dilutions of $5e^{-3}$ were dried to the slide. The crimson microbeads were

used to measure wavefront aberrations while yellow-green microbeads were imaged before and after correction using the Andor camera.

Figure 9.9 shows the wavefront aberrations before and after correction and a horizontal profile across the diameter of each is shown in Figure 9.10. The RMS error of the wavefront before correction compared to a perfectly flat wavefront was determined to be $0.4254\mu\text{m}$. A final RMS error of $.0572\mu\text{m}$ was achieved after seven iterative corrections. A $0.2\mu\text{m}$ diameter microbead was imaged before and after correction using the Andor camera. Figure 9.11 displays an image X-Y plane of the microbead before and after correction according to the orientation in Figure 9.12. Figure 9.13 compares the X-Z profile of the microbead before and after correction with an ideal PSF. Correction of wavefront aberrations resulted in a two-fold increase in the maximum intensity. As shown in the Figures 9.11 and 9.13, the PSF of the microbead is significantly improved.



a) b)
Figure 9.9: Induced aberrations before (a) and after (b) correction

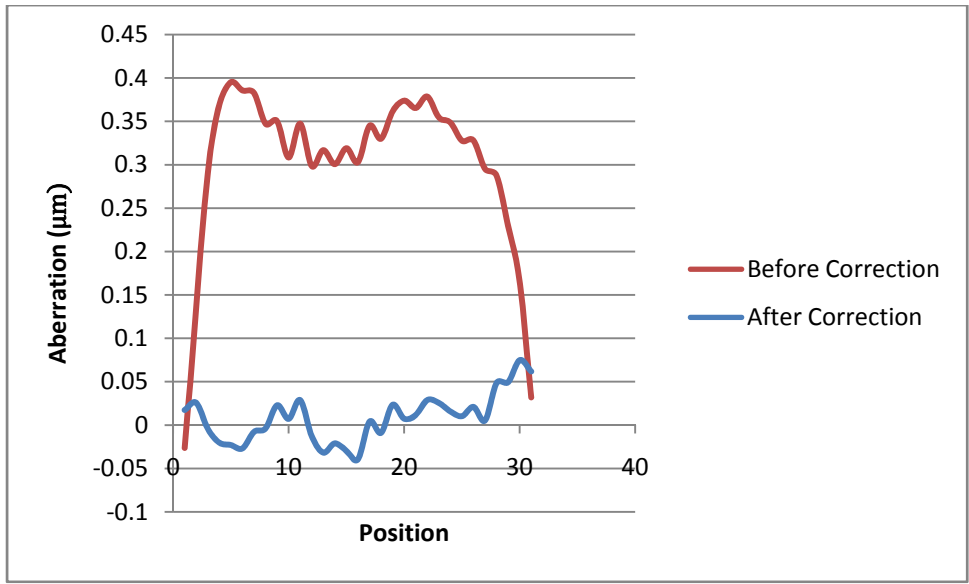


Figure 9.10: Horizontal profile of wavefront before and after correction of induced aberrations

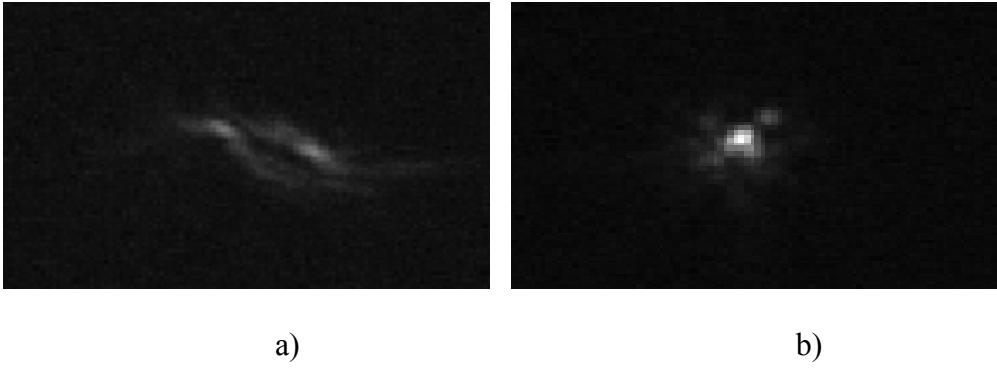


Figure 9.11: X-Y plane of 0.2 μm diameter Y-G microbeads before (a) and after (b) correction

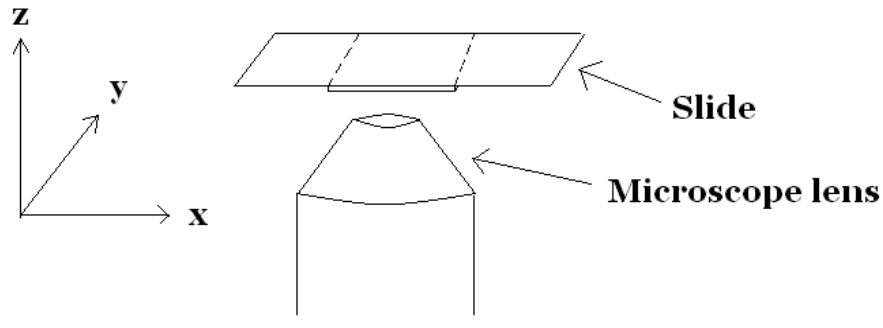
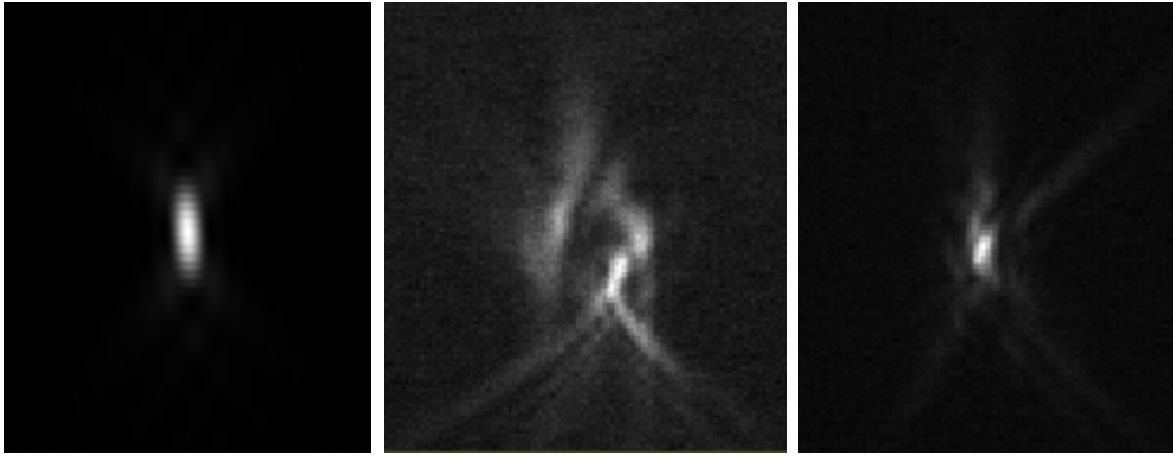


Figure 9.12: Axis orientation



a) b) c)
Figure 9.13: PSF comparison in X-Z plane of Ideal PSF (a), 2 μm diameter Y-G microbeads before (b) and after (c) correction.

CHAPTER 10:

Measurement and correction of Aberrations in *C. elegans*

Preparation of *C. elegans* samples

The *C. elegans* strains used in this study were provided by Dr. Adrian Wolstenholme's lab. Dr. Wolstenholme is a member of the Department of Infectious Diseases at the University of Georgia. For this study, the RK-1 and NM-440 strains were used. These strains express GFP in the cytoplasm of the nerve cells in the nerve ring, ventral cord, and dorsal cord. The following steps were followed to prepare *C. elegans* samples. Wavefront aberrations caused by *C. elegans* were measured using fluorescent microbeads fixed below the roundworms. Twenty microliters of a dilution of $1e^{-4}$ crimson fluorescent microbeads were dried onto the microscope slide. Fifteen microliters of a half and half mixture of M9 buffer solution and 1% Azide was then applied to the slide. Azide is used as a paralyzing agent. Using inoculating loops, worms were transferred from the growth plate to the slide. 15 micro-liters of mounting solution was then applied, followed by the cover slip.

Measurement and Correction using Microbeads as "Guide Stars"

To acquire the baseline Shack-Hartmann image, a separate slide containing microbeads fixed to the cover slip was used. All preprocessing of the baseline image, including determining the Shack-Hartmann spots was completed before examination of the *C. elegans* sample. The offset image was obtained by exciting a microbead fixed beneath a roundworm with the Thorlabs S1FC635 laser. The resulting wavefront is shown in Figure 10.1. As seen in the Figure, spherical type aberrations are induced by the roundworm, most likely due to the varying

refractive indices of the varying types of tissue in the worm as well as its three dimensional shape. A horizontal profile of the wavefront aberrations in Figure 10.1 is shown in Figure 10.2. The correction goal of $.066\mu\text{m}$ RMS was not reached for the *C. elegans* samples tested. A final RMS error of $.224\mu\text{m}$ was achieved, which is an improvement to the $0.471\mu\text{m}$ RMS error before correction. The images in Figure 10.3 were acquired using the Andor camera and display the worm before and after correction. An x-profile of the worm before and after correction (Figure 10.4) shows the increase in signal intensity from correction with the Adaptive Optic system.

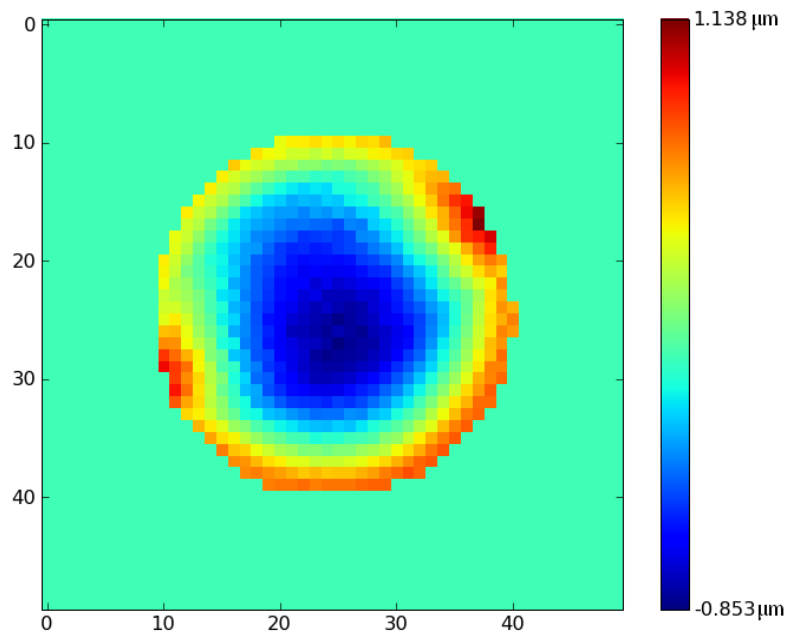


Figure 10.1: Aberrations caused by *C. elegans*. Measured with $1\ \mu\text{m}$ diameter crimson bead fixed beneath sample.

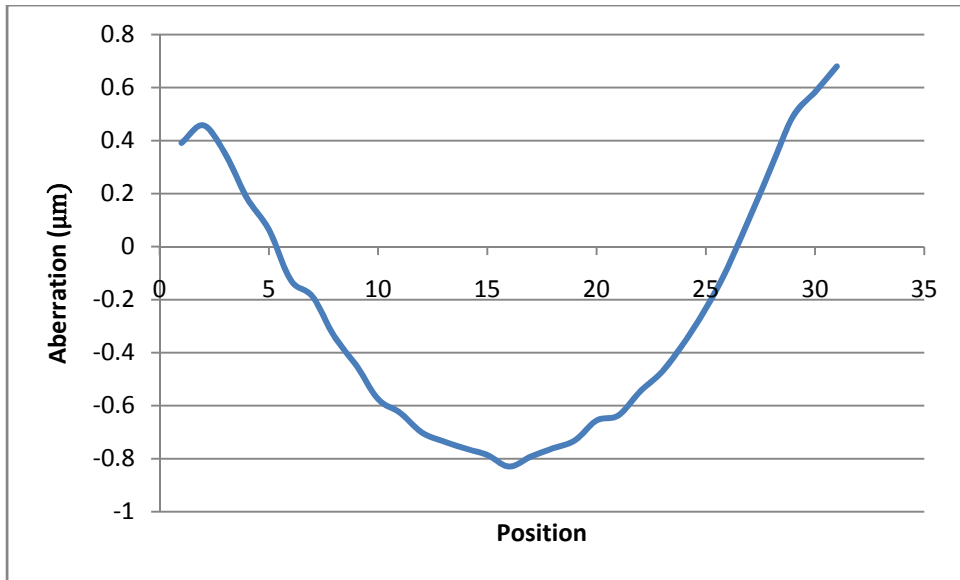
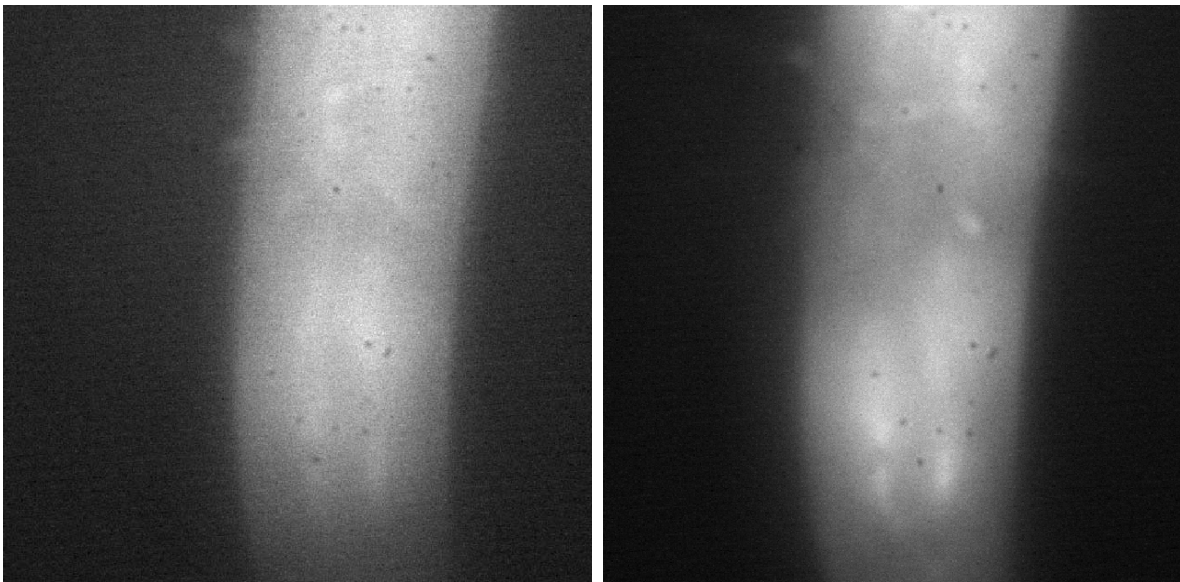


Figure 10.2: Horizontal Profile of wavefront aberrations caused by *C. elegans*.



a) **Figure 10.3:** *C. elegans* before (a) and after (b) correction

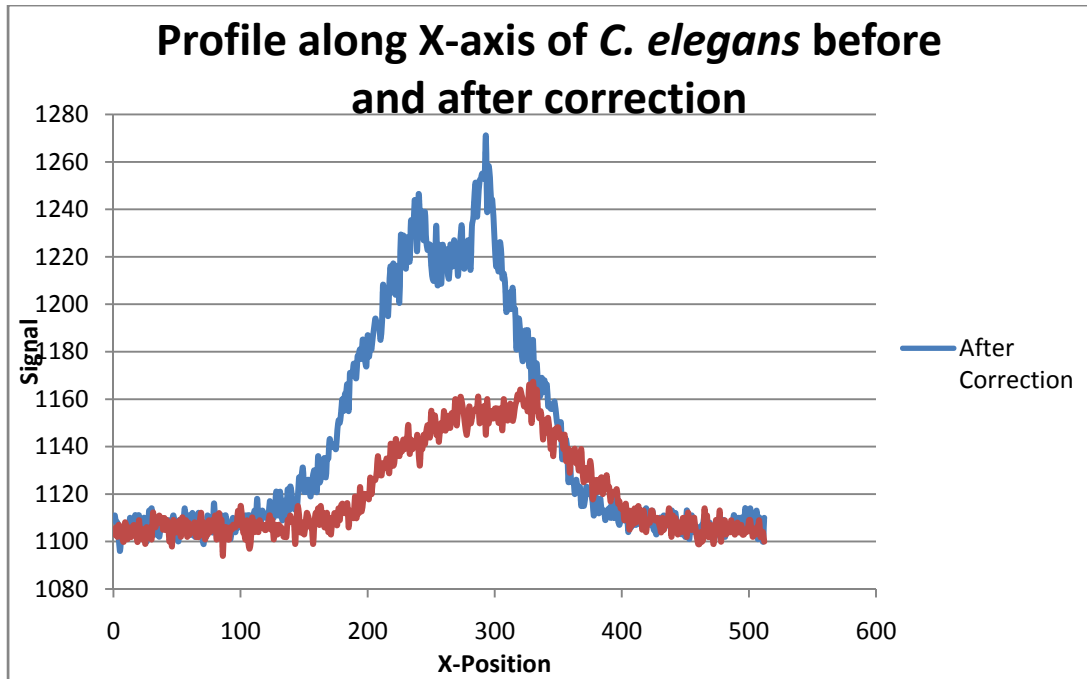


Figure 10.4: *C. elegans* signal across x-axis before and after correction

Wavefront Measurement using GFP

In order to use GFP as the signal source for the offset Shack-Hartmann image, the configuration of the Cyan laser was changed to produce a confocal spot at the microscope slide. A baseline image of 1 μ m diameter YG microbeads fixed to the coverslip was obtained in the same manner as in Chapters 8 and 9, but with the Cyan laser as the excitation source. Offset Shack-Hartmann images were taken using the GFP as the signal source. An example of an offset image acquired from the GFP expressed by the worm is shown as Figure 10.5. To image the Yellow Green microbeads and GFP onto the Photometrics HQ2 camera, D3 was removed from the optical setup (Figure 9.1) and replaced with a beam splitter. An example of the wavefront aberrations measured using GFP as a signal source for the Shack-Hartmann sensor is shown in Figure 10.6.

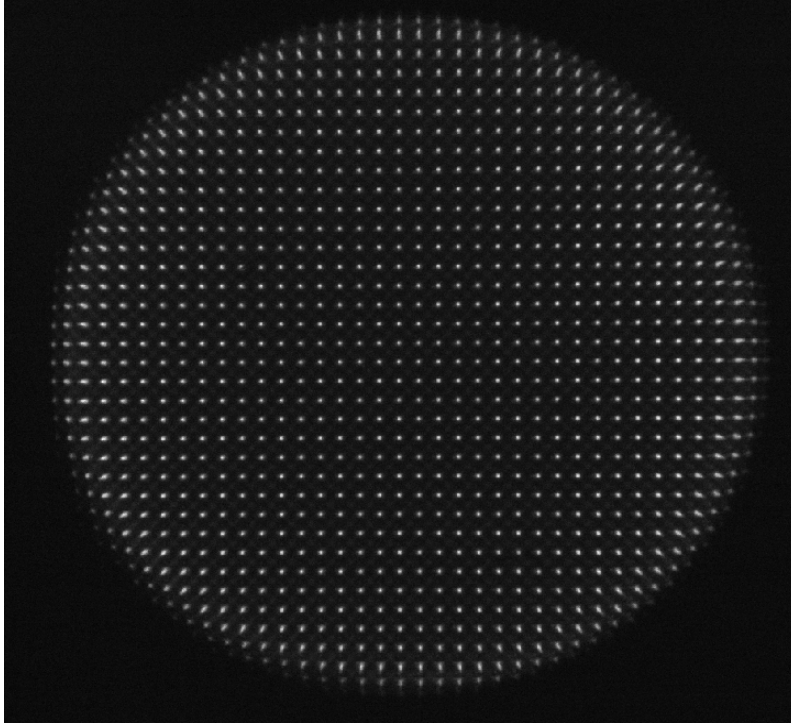


Figure 10.5: Offset Shack-Hartmann image with GFP as the signal source

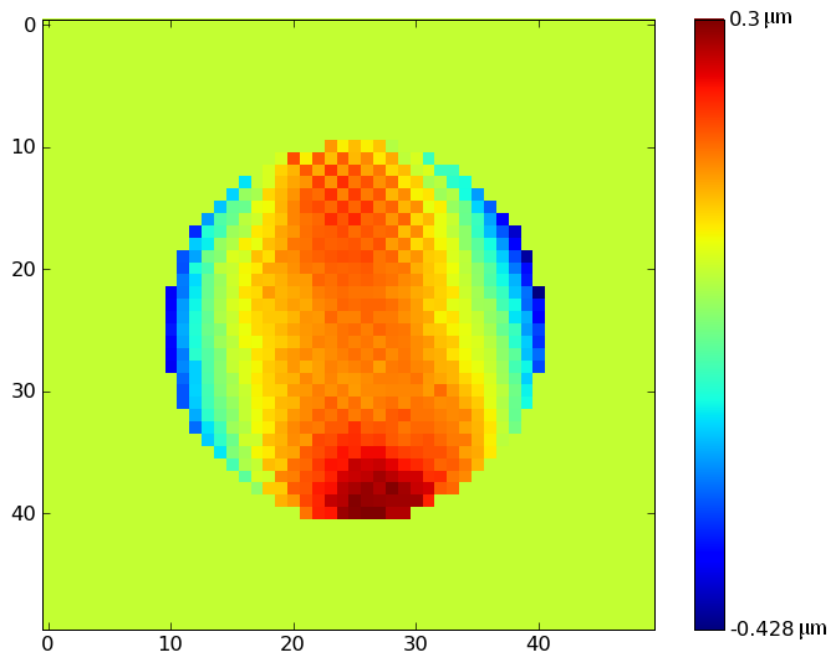


Figure 10.6: Wavefront aberrations measured using GFP as signal for Shack-Hartmann sensor.

The final data presented in this study involved measuring the wavefront aberrations using a specifically labeled organ in *C. elegans*. For the NM-440 strain of *C. elegans* we measured the wavefront aberrations using GFP expressed in the cells of the nerve ring shown in Figure 10.7. The baseline image was taken of a bead fixed to the coverslip as discussed in the previous experiments. The measured wavefront aberrations using fluorescence from the nerve ring of the *C. elegans* sample is shown in Figure 10.8. The RMS error when compared to a perfectly flat wavefront is $0.227\mu\text{m}$. Comparing Figures 10.6 and 10.8 it is apparent that the wavefront aberrations change greatly from worm to worm, making dynamic measurement and correction necessary.

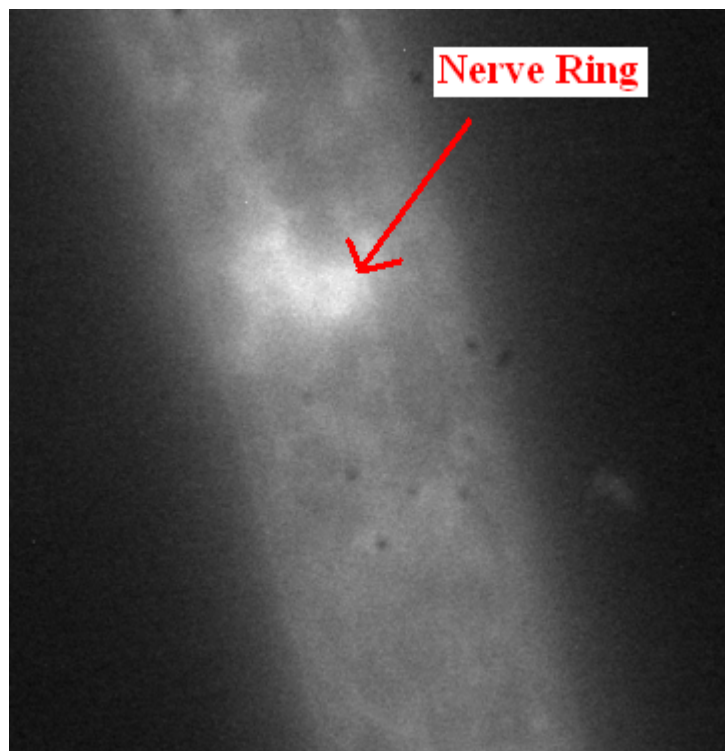


Figure 10.7: *C. elegans* nerve ring used for measuring wavefront aberrations

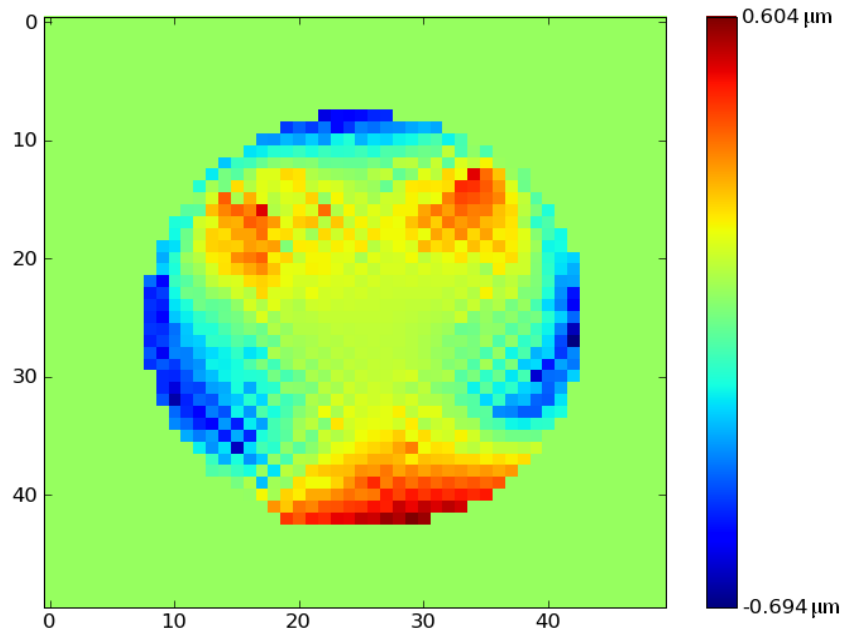


Figure 10.8: Wavefront measured using GFP expressed by cells in the nerve ring of *C. elegans*

Chapter 11

Conclusions

We have demonstrated a method for wavefront aberration correction in a wide-field fluorescence microscope with adaptive optics. Direct measurement of the wavefront was accomplished using fluorescent microspheres fixed beneath the sample as the reference source for a Shack-Hartmann Sensor and correction was applied with a deformable mirror. We demonstrated the ability to correct for aberrations caused by defocusing and focusing into a sample with an index of refraction mismatch. Although we were unable to reach the correction goal of a 0.066 RMS for *C. elegans* samples, an improvement in overall signal and image quality was obtained.

We successfully utilized GFP as a signal source for the Shack-Hartmann Wavefront Sensor. This opens the possibility for correction of specific GFP labeled organs within a sample. Using GFP as a sensor signal also simplifies the measurement process and represents an important step to making this technology accessible and practical for wide spread use.

Future work on this project involves increasing the degree of correction for biological samples. We will be investigating several different wavefront reconstruction algorithms as well as determining if errors are being induced through the centroiding algorithm and influence function array. This work represents an important step to our future goals of a wide-field fluorescence microscopy system that is capable of producing high-resolution, corrected images of live biological samples.

REFERENCES

1. Hardy, J.W. 1998. *Adaptive Optics for Astronomical Telescopes*. New York, N.Y.: Oxford University Press.
2. Max, C., University of California at Santa Cruz, Astronomy 289C.
3. Booth, M. J., Neil, M. A. A., Juskaitis, R., and T. Wilson. 2002. Adaptive aberration correction in a confocal microscope. *PNAS*. Vol. 99, p.5788-5792.
4. Sherman, L., Ye, J. Y. , Albert, O., Norris, T.B. 2002. Adaptive correction of depth-induced aberrations in multiphoton scanning microscopy using a deformable mirror. *J. Microscopy*. Vol. 206, p.65-71
5. Neil, M. A. et al. 2000. Adaptive aberration correction in a two-photon microscope. *Journal of Microscopy*. Vol. 200, p.105-108.
6. Kner, P., Sedat, J. W., Agard, D. A., Kam, Z. 2009. High-resolution wide-field microscopy with adaptive optics for spherical aberration correction and motionless focusing. *Journal of Microscopy*.
7. Azucena, O. et al. 2010. Wavefront aberrations measurements and corrections through thick tissue using fluorescent microsphere reference beacons. *Optics Express*. Vol. 18. p. 17522-17532.
8. Kaletta, T., Hengartner, M. O. 2006. Finding function in novel targets: *C. elegans* as a model organism. *Nature Reviews Drug Discovery*.
9. Gualda, E. J. et al. 2007. *In vivo* imaging of anatomical features of the nematode *Caenorhabditis elegans* using non-linear (TPEF-SHG-THG) microscopy. *Proc. Of SPIE-OSA Biomedical Optics*. Vol. 6630.
10. Babcock, H. W. 1953. The possibility of compensating astronomical seeing. *Publications of Astronomical Society of the Pacific*, Vol. 65, No.385, p.226.
11. Tyson, R.K. 1998. *Principles of Adaptive Optics*. London: Academic Press

12. Freeman, R. H., and J. E. Pearson. 1982. Deformable mirrors for all seasons and reasons. *Applied Optics*. Vol. 21, p-580-588.
13. Kam, Z. et al. 2006. Modeling the application of adaptive optics to wide-field microscope live imaging. *Journal of Microscopy*. Vol. 226, p.33-42.
14. Katz, M. 1994. *Geometrical Optics*. London: World Scientific.
15. Goodman, J. W. 2005. *Introduction to Fourier Optics*.
16. Born, M., and E. Wolf. 1965. *Principles of Optics*. New York: Pergamon
17. Noll, R. J. 1975. Zernike polynomials and atmospheric turbulence. *J. Opt. Soc. Am.*, Vol. 66, p.207-211.
18. Booth, M. J. 2007. Adaptive optics in microscopy. *Phil. Trans. R. Soc.*, Vol. 365, p.2829-2843.
19. Marsh, P.N., Burns, D., and J.M. Girkin. 2003. Practical implementation of adaptive optics in multiphoton microscopy. *Optics Express*. Vol. 11, p.1123-1130
20. Foucault, L. "Description des procedes employes pour reconnaitre la configuration des sufaces optiques," *Comptes rendus hebdomadaires des séances de l'Academie des Sciences, Paris*, vol. 47, p. 958-959.
21. F. Roddier, *Appl. Opt.*, 27, 1223, 1988
22. Neil, M. A. A., Booth, M. J., Wilson, T. 2000. Closed-loop aberration correction by use of a modal Zernike wave-front sensor. *Optics Letters*.
23. Aksenov, V.P., and Y. N. Isaev. 1992. Analytical representation of the phase and its mode components reconstructed according to the wave-front slopes. *Optics Letters*. Vol. 17, p.1180-1182.
24. The *C. elegans* Sequencing Consortium. 1998. Genome sequence of the nematode *C. elegans*: a platform for investigating biology. *Science*. Vol. 282, p. 2012-2018
25. Wormclassroom.org. Accessed August 2nd, 2011

26. Albert, O., Sherman, L., Mourou, T. B., and G. Vdovin. 2000. Smart Microscope: an adaptive optics learning system for aberration correction in multiphoton confocal microscopy. *Optics Letters*. Vol 25, p. 52-54.
27. Rueckel, M., Mack-Bucher, J. A., and W. Denk. 2006. Adaptive wavefront correction in two-photon microscopy using coherence-gated wavefront sensing. *PNAS*. Vol 46, p. 17137-17142.
28. Denk W, Strickler J, Webb W (1990). "Two-photon laser scanning fluorescence microscopy". *Science* Vol. 248, p. 73–6.
29. Goepfert-Mayer M 1931. Über Elementarakte mit zwei Quantensprüngen. *Ann Phys* **9**, Vol. 3, p. 273–95.
30. Tao, X. et al. 2011. Adaptive optics confocal microscopy using direct wavefront sensing. *Optics Letters*. Vol 36 p. 1062-1064.
31. Luke, D. R., J. V. Burke, and R. G. Lyon. Optical wavefront reconstruction: theory and numerical methods. *Society for Industrial and Applied Mathematics*. Vol. 44, p.169-224
32. Fried, D. L. 1976. Least-square fitting a wave-front distortion estimate to an array of phase-difference measurements. *J. Opt. Soc. Am.* Vol. 67, p.370-375.
33. Guo, H. and Z. Wang. 2005. Wavefront reconstruction using iterative discrete Fourier transforms with Fried geometry. *Optik*. Vol. 117, p.77-81.
34. Hermann, J., 1980. Least-squares wavefront errors of minimum norm. *J. Opt. Soc. Am.* Vol.70, p. 22-35.
35. Poyneer, L. A., Gavel, D. T., and J. M. Brase. 2002. Fast wave-front reconstruction in large adaptive optics systems with use of the Fourier transform. *J. Opt. Soc. Am.* Vol. 19, p.2100-2111.
36. Hunt, B. R. 1978. Matrix formulation of the reconstruction of phase values from phase differences. *J. Opt. Soc. Am.* Vol. 69, p.393-399.
37. Freischlad, K. R. and C. L. Koliopoulos. 1986. Modal estimation of a wave front from difference measurements using the discrete Fourier transform. *J. Opt. Soc. Am.* Vol. 3, p.1852-1861.

38. Aksenov, V.P., and Y. N. Isaev. 1992. Analytical representation of the phase and its mode components reconstructed according to the wave-front slopes. *Optics Letters*. Vol. 17. p.1180-1182.
39. Gavel, D. T., 2003. Suppressing anomalous localized waffle behavior in least-squares wavefront reconstructors. *SPIE*.
40. Kner, P., Winoto, L., Agard, D. A., and J. W. Sedat. 2010. Closed loop adaptive optics for microscopy without a wavefront sensor. *SPIE*. Vol. 7570.
41. Hanser, B. M., Gustafsson, M. G., Agard, D. A., and J. W. Sedat. 2003. Phase retrieval for high-numerical-aperture optical systems. *Optics Letters*. Vol. 28, p. 801-803.